Fuel xxx (xxxx) 132325

Contents lists available at ScienceDirect

Fuel

journal homepage: www.elsevier.com/locate/fuel

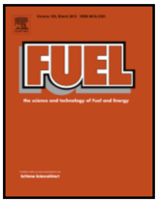

Full Length Article

A comprehensive numerical investigation on spray models for Direct-Injection Spark-Ignition engines

Diego Bestel [a], Joohan Kim [a], Le Zhao [b,*], Anqi Zhang [b], Ji-Woong Park [b], Fabien Tagliante [c], Lyle Pickett [c], Muhsin Ameen [a], Roberto Torelli [a,*]

[a] Transportation and Power Systems Division, Argonne National Laboratory, Lemont, IL 60439, USA
[b] Aramco Americas: Aramco Research Center – Detroit, Novi, MI 48377, USA
[c] Combustion Research Facility, Sandia National Laboratories, Livermore, CA 94551, USA

ARTICLE INFO

Keywords:
Spray modeling
Free-spray behavior
ECN Spray G
Gasoline direct injection
Spray model calibration

ABSTRACT

Gasoline direct-injection spark-ignition (DISI) engines generate a large portion of their unburned hydrocarbon (UHC) and soot emissions during the cold-start phase. A predictive computational fluid dynamics (CFD) modeling framework can be used to understand the physical processes that characterize fuel spray evolution and fuel-film formation at cold start conditions, which can help to reduce engine-out particulate emissions. This study systematically evaluated spray submodels and developed a set of simulation best practices for physical-numerical submodels with the goal of enabling accurate simulations of liquid spray behavior in a DISI engine. Three comprehensive experimental datasets containing free-spray projected liquid volume (PLV), liquid volume fraction (LVF), and near-field X-ray radiography data were used to validate the simulation results and evaluate the spray submodels. Systematic analysis delved into injected parcel distribution, droplet collision, spray breakup, and evaporation via a detailed assessment of the relevant spray submodels. Moreover, the effects of turbulence models and the initial turbulent flow properties on the liquid spray evolution were examined. Based on extensive calibration efforts, a set of simulation best practices for the free spray was developed and validated against the PLV/LVF data. Simulation results indicated that the uniform distribution for parcel initialization, coupled with appropriate droplet collision submodels, provides an improved spray morphology compared to the cluster distribution. The findings also underscored the importance of calibrating the Kelvin-Helmholtz Rayleigh-Taylor (KH-RT) breakup model constants and droplet heat transfer coefficient scaling factor to achieve favorable agreement regarding measured liquid penetration and spray widths. This study marks a substantial stride towards accurately predicting fuel film evolution and soot formation within DISI engine performance.

1. Introduction

Direct-injection spark-ignition (DISI) engines are widely employed in light-duty vehicles due to their potential for enhanced thermal efficiency and improved cold-start combustion stability in comparison to port fuel injection (PFI) engines [1,2]. Nevertheless, under cold conditions, direct injection can lead to undesirable fuel-film wetting on the combustion chamber's walls due to the reduced fuel evaporation rate, resulting in relatively higher particulate emissions when compared to port fuel injection engines [3]. It has been demonstrated that a substantial portion of particulate matter and particulate number emissions ($>$ 70 %) are emitted when the engine is not yet fully warmed up [4]. The major sources of particulate emissions have been identified as fuel-film wetting [5], inhomogeneous air–fuel mixture distribution [6], and injector tip deposition [7]. To address these concerns and reduce particulate emissions in DISI engine-powered vehicles, advanced injection systems that allow high-pressure injection to achieve better fuel atomization [8] and/or enable multiple injections to shorten the liquid spray penetration [9] have been proposed.

Computational fluid dynamics (CFD) simulations play a crucial role in understanding the dynamic evolution of the fuel spray within the combustion chamber and guiding the development of optimal injection strategies to mitigate engine-out particulate emissions. However, the reliability of such simulation-based analysis and optimizations depends on the accuracy and predictiveness of submodels. While spray models for diesel sprays have been extensively studied and calibrated, there exists a significant gap in the comprehensive understanding of gasoline direct-injection (GDI) sprays, particularly under cold conditions

---

[*] Corresponding authors.
E-mail addresses: le.zhao@aramcoamericas.com (L. Zhao), rtorelli@anl.gov (R. Torelli).

https://doi.org/10.1016/j.fuel.2024.132325
Received 28 February 2024; Received in revised form 7 June 2024; Accepted 22 June 2024
0016-2361/© 20XX

Table 1
Summary of experimental conditions used for model validation and submodels evaluation. Note that the X-ray radiography conditions are similar to those of the standard Spray G1 [23], except for the vessel temperature and, consequently, density.

Experimental Condition	Fuel	Vessel Temperature (K)	Vessel Pressure (bar)	Vessel Density (kg/m^3)	Inj. Temperature (K)	Inj. Pressure (bar)	Inj. Duration (μs)	Inj. Mass (mg)
PACE (DBI)	Co-Optima E30	587	8.0	4.64	363	170	1043	13.8
Spray G1 (X-ray)	*iso*-octane	298	6.0	6.80	363	200	780	10.0

[10–12]. The distinctive challenges presented by GDI sprays during cold start scenarios necessitate a closer examination of their behavior, considering factors such as reduced evaporation rates and the consequent impact on fuel-film formation [5,13,14].

Therefore, a comprehensive validation of spray submodels using high-fidelity experimental data becomes crucial. Spray-wall interaction significantly governs the generation of locally fuel-rich mixtures and the formation of fuel-film wetting, prompting extensive research efforts to thoroughly validate submodels dedicated to capturing the behavior of free spray. This stepwise approach ensures that the impact of spray-wall interaction on engine performance is comprehensively understood and accurately represented in the simulation models [9,15–19]. The validations of spray submodels are typically carried out using data acquired from spray vessel experiments before integrating them into engine simulations.

Many researchers [9,15–17] have compared simulation results with experimental data, often relying on high-speed Mie-scattering images for the analysis of liquid penetration and spray morphology. However, it is important to note that high-speed Mie-scattering images, while valuable, present uncertainties arising from pixel-based light intensity thresholding, making quantitative comparisons between experimental data and simulations challenging. As an alternative approach, recommended by the Engine Combustion Network's (ECN), researchers have adopted the use of projected liquid volume (PLV) for liquid spray char-

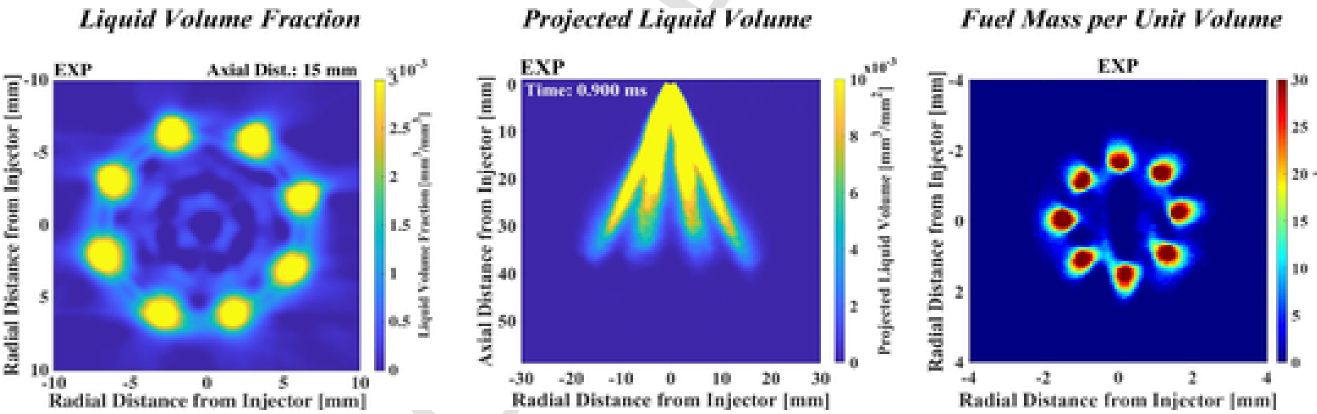

Fig. 1. Examples of experimental Liquid Volume Fraction (left), Projected Liquid Volume (center), and fuel mass per unit volume (right) used for simulation results validation and spray submodels evaluation. Note that fuel density in the X-ray radiography data is the measured fuel mass per unit volume, not the physical property density.

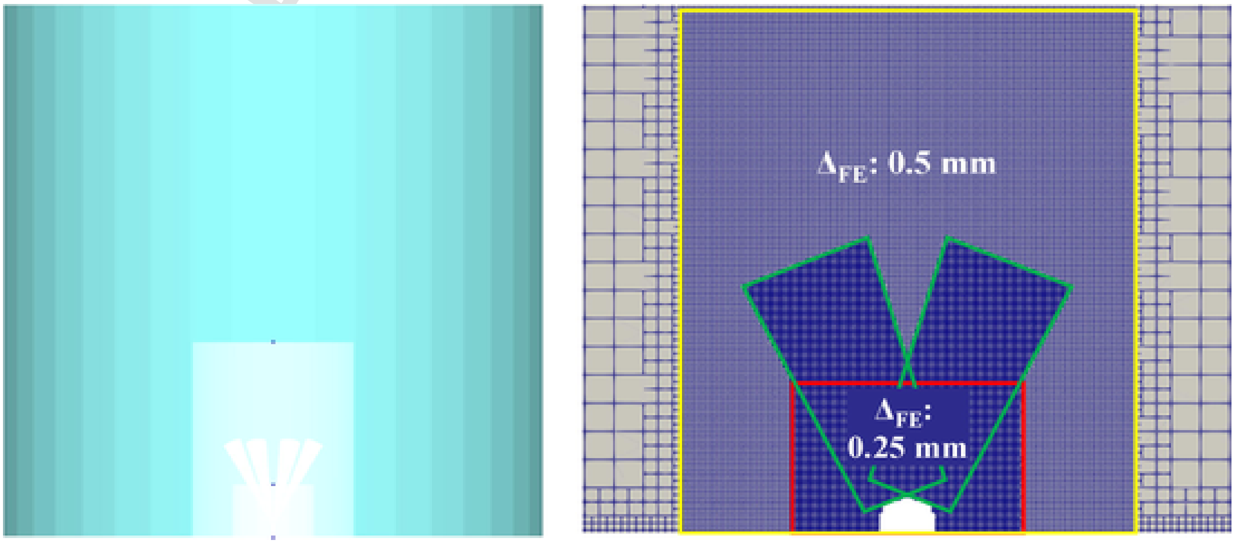

Fig. 2. Simplified internal volume of spray vessel (left); Computational grid configuration (right).

Table 2
7-component fuel surrogate composition.

Name	Formula	Composition (m/m)
n-pentane	$n\text{-}C_5H_{12}$	4.53 %
iso-pentane	$iso\text{-}C_5H_{12}$	8.92 %
2,2,4-trimethylpentane (*iso*-octane)	$iso\text{-}C_8H_{18}$	14.98 %
1-hexene	C_6H_{12}	19.49 %
Tetralin	$C_{10}H_{12}$	7.02 %
1,2,4-trimethylbenzne	C_9H_{12}	12.68 %
Ethanol	C_2H_5OH	32.38 %

Table 3
Comparison of physical properties between Co-Optima E30 (real fuel) and 7-component fuel surrogate.

Parameters	Real fuel	Surrogate fuel
Density @ 15 °C [kg/m^3]	752.7	741.8
Research octane number [-]	97.9	98.6
Motor octane number [-]	87.1	86.2
Low heating value [MJ/kg]	38.2	38.2
Distillate temperature [°C]		
T5	55.0	52.1
T10	60.5	53.8
T20	66.4	61.7
T30	70.1	71.2
T40	72.5	75.9
T50	74.3	77.8
T60	75.7	83.0
T70	78.3	89.5
T80	134.1	113.8
T90	155.0	163.5
T95	176.0	181.8

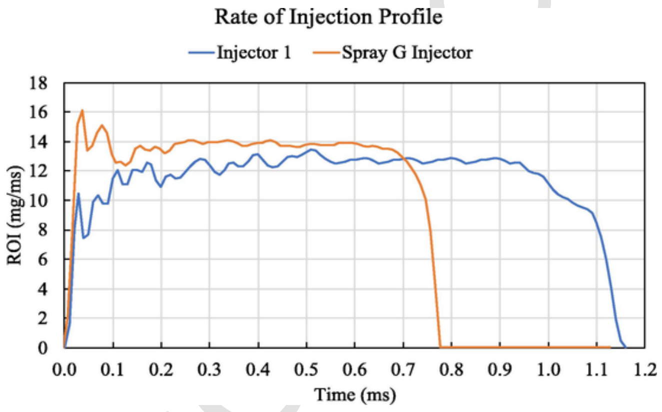

Fig. 3. Injection pressure profiles for the Injector 1 (blue) and Spray G injector (orange). (For interpretation of the references to colour in this figure legend, the reader is referred to the web version of this article.)

Table 4
Investigated models and constant ranges.

Physics	Baseline	Ranges
Injected Parcel Distribution	Uniform	Uniform, Cluster
Droplet Collision Model	O'Rourke	O'Rourke, NTC
Droplet Collision Outcome Model	O'Rourke	O'Rourke, Post
KH breakup: B_1 constant	5.0	10, 24, 35, 50
KH breakup: Shed Factor	0.1	0.1, 0.5, 1.0
RT breakup: C_{RT}	0.6	0.1, 0.5, 1.0, 5.0

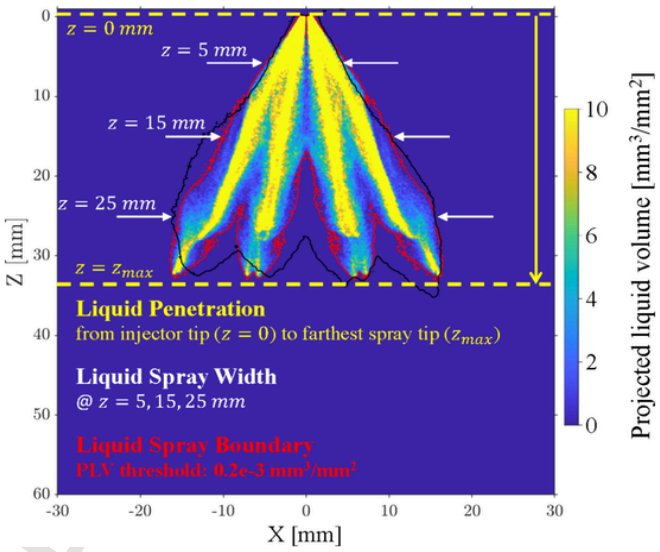

Fig. 4. Selected PLV contour from simulation results illustrating the definitions of Liquid Penetration Length (LPL) and Liquid Full Widths (LFW) used for model validation.

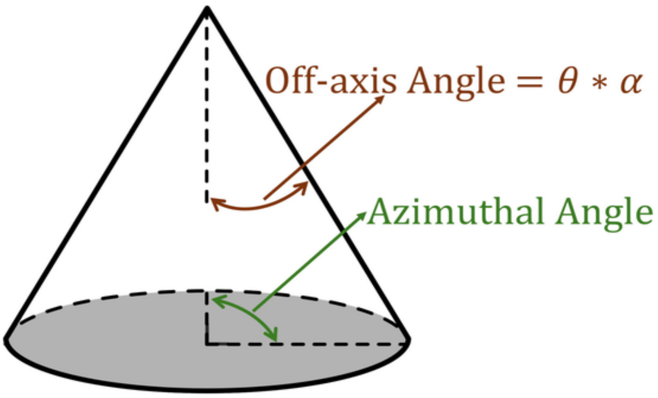

Fig. 5. Illustration of the off-axis and azimuthal angles used to define the droplet velocity components. The calculation of the off-axis angle depends on the distribution chosen.

acterization [20]. PLV is measured through diffused back illumination (DBI) extinction imaging and aligns directly with the simulation results, eliminating arbitrary thresholding. Consequently, PLV-based submodel validation becomes more relevant, enabling accurate identification of simulation-experiment disparities for enhanced model refinement [21, 22]. In this study, PLV and liquid volume fraction (LVF) data obtained from DBI technique [23] are leveraged to conduct a comprehensive assessment of the sensitivity of spray simulation results to various spray submodels and their associated constants. Additionally, X-ray radiography data [24] is employed to enhance the model evaluation, with a particular focus on the near-nozzle region.

The primary goal of this research is to develop a set of simulation best practices for physical-numerical submodels to ensure accurate predictions of liquid spray and fuel-film characteristics in a DISI engine. This effort not only introduces the simulation best practices but also entails a systematic exploration of different responses and sensitivities exhibited by various spray submodels, along with their calibration. This paper serves as the initial phase in a continuous endeavor aimed at the comprehensive calibration and validation of spray submodels for GDI sprays under cold conditions. Subsequent sections will discuss the experimental and numerical setups, evaluate several spray submodels, and establish the set of simulation best practices. Finally, the conclusion will provide a summary of the insights gained in this study.

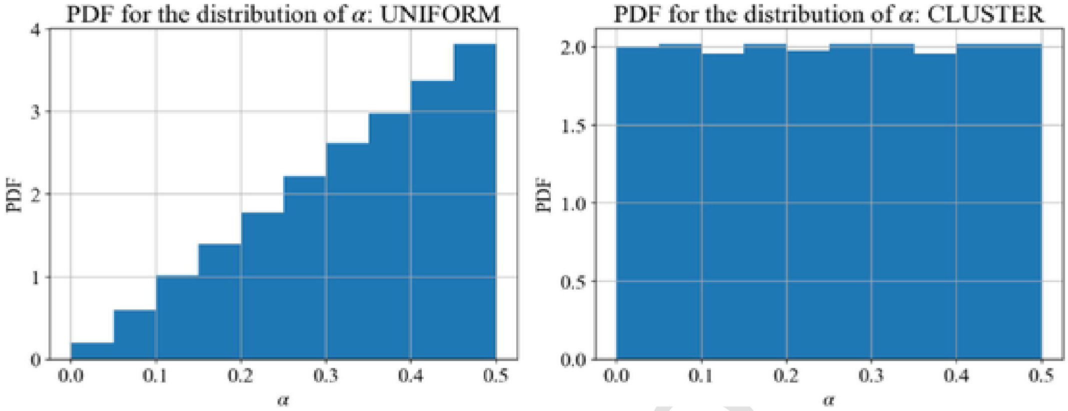

Fig. 6. Probability density functions of α for the "uniform" (left) and "cluster" (right) distributions. As can be seen, the "uniform" distribution favors larger α, which results in droplets being distributed across a larger cross sectional area of the plume. The "cluster" distribution, on the other hand, offers a more homogeneous distribution of α, which results in droplets being distributed in a smaller cross sectional area of the plume.

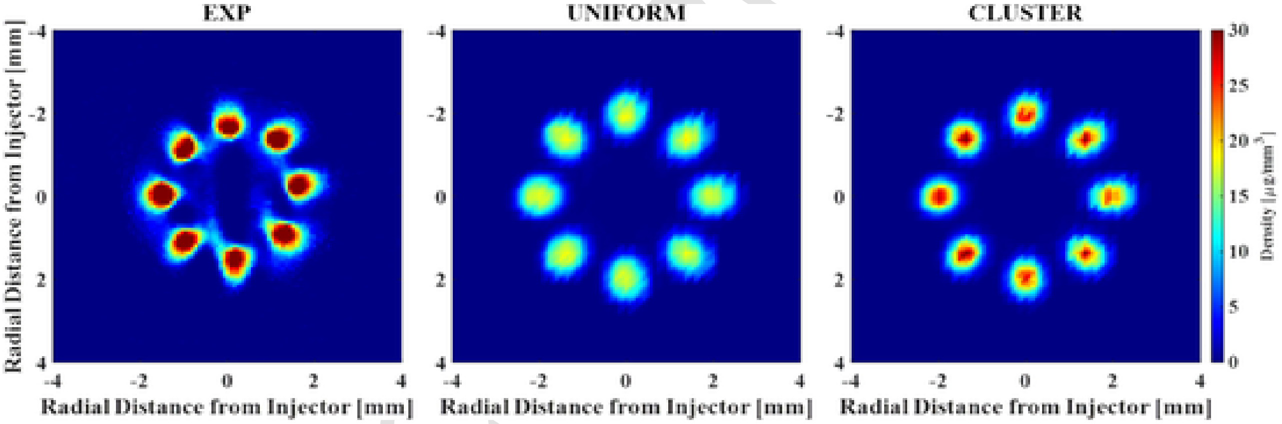

Fig. 7. Experimental X-ray radiography results of the Spray G injector (left), fuel density simulation results from the "uniform" (center) and "cluster" (right) distributions. As expected, the "cluster" distribution case shows an increased fuel mass in the plume center, whereas the "uniform" distribution shows a more uniform fuel mass distribution.

2. Experimental setup

Two injector models were used in this study: (1) Injector 1, based on the model used in the Co-Optimization of Fuels and Engines and Partnership for Advanced Combustion Engines (PACE) programs of the U.S. Department of Energy, and (2) the Spray G injector model from the ECN. The following sections provide the detailed descriptions of these two injectors, their respective experimental setups, and the corresponding test conditions.

2.1. Injector 1

Spray tests were performed in an optically accessible, constant-flow, constant-pressure spray vessel at Sandia National Laboratory. While the experimental apparatus and the imaging techniques were discussed in detail in prior work [23], a summary is presented here. A valve-covered orifice solenoid injector was utilized for fuel injection, i.e., Injector 1. This injector has eight stepped holes with a 0.14 mm diameter and 0.36 mm counterbore diameter, and the orifice drill angle is 26.5° relative to the nozzle axis. Detailed information about the injector geometry and specifications can be found elsewhere [25]. The injection pressure was 170 bar, and the electrical injection duration was 1043 μs, delivering 13.8 mg of fuel mass. The ambient thermodynamic condition of the vessel was intended to replicate in-cylinder conditions at the start of the injection (SOI), namely 582 K and 8 bar. Note that after the start of injection, the pressure and temperature increase in the engine combustion chamber due to the piston compression; however, this transient effect is not considered in the spray experiments.

Liquid spray behavior was characterized using the PLV through DBI extinction imaging. The injector was rotated to many different perspectives to obtain a tomographic reconstruction of the three-dimensional Liquid Volume Fraction (LVF) as indicated in Eq. (1). Side-view extinction imaging was also featured in a rotation where the liquid sprays from four holes overlapped with the plumes from the other four holes along the line of sight. The measured light intensity was used to compute the optical thickness (τ) of the liquid spray, and the PLV and LVF were computed as follows,

$$PLV = \tau \frac{\pi d^3/6}{C_{ext}} = \int_{-y_\infty}^{y_\infty} LVF \, dy \tag{1}$$

where d is droplet diameter and C_{ext} is the extinction coefficient, assuming these values remained constant along the line of sight. In this study, a Sauter mean diameter (SMD) of 10 μm and a C_{ext} of 77.806·10^{-6} mm^2 [26] were used for calculating the experimental PLV field. It is worth noting that these recommended values for SMD and C_{ext} are larger than those used in previous studies of gasoline Spray G [23]. This

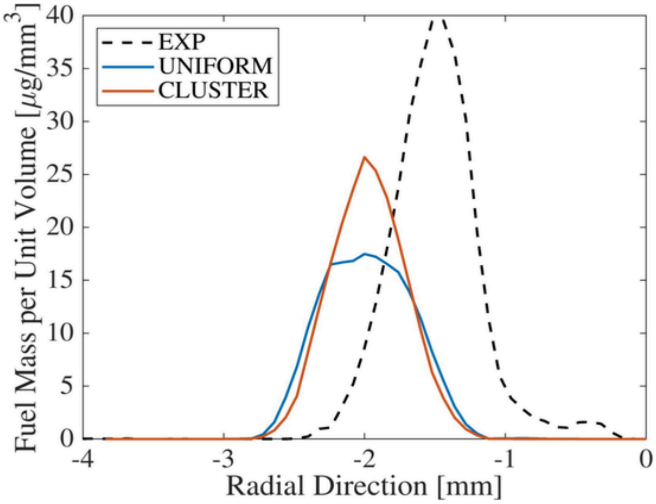

Fig. 8. Fuel mass per unit volume radial profiles of the horizontally-left-most plume. Although the “cluster” distribution shows improved results in fuel mass towards the plume center, both distributions fail to accurately reproduce the experimental results with the baseline spray model calibration.

adjustment is based upon an improved understanding of droplet scattering effects when using diffused lighting [27].

2.2. *Spray G injector*

Similarly to Injector 1, the Spray G injector is also a valve-covered orifice solenoid injector with eight holes. The inner diameter of the nozzle hole is 0.165 mm, and the counterbore diameter is 0.388 mm. The orifice drill angle is 37° from the center axis. More details of the injector geometry can be found in the original work [23]. The injection and vessel thermodynamic conditions for the Spray G injector are provided in Table 1.

Since the DBI technique is known to yield higher uncertainties in regions of high liquid density [23,24,28], a modified Spray G1 test condition containing time-resolved X-ray radiography measurements of the near-field fuel mass per unit volume distribution [24] was utilized in this study to validate the spray submodels in the near-field region. In these measurements, the vessel temperature was maintained at room temperature of 298 K due to experimental apparatus restrictions. Details about the experimental apparatus, the principles of X-ray radiography, and associated techniques can be found in the literature [24, 28–31]. Fig. 1 illustrates the visual representations of LVF, PLV, and fuel mass per unit volume distribution used in this work.

3. Numerical setup

Simulations were conducted using the CONVERGE code version 3.0 [32], a commercial solver that automates the mesh generation process and allows the use of simple orthogonal grids, fixed embedding (FE), and adaptive mesh refinement (AMR). A co-located finite volume approach was used to compute the conservation equations of mass, mo-

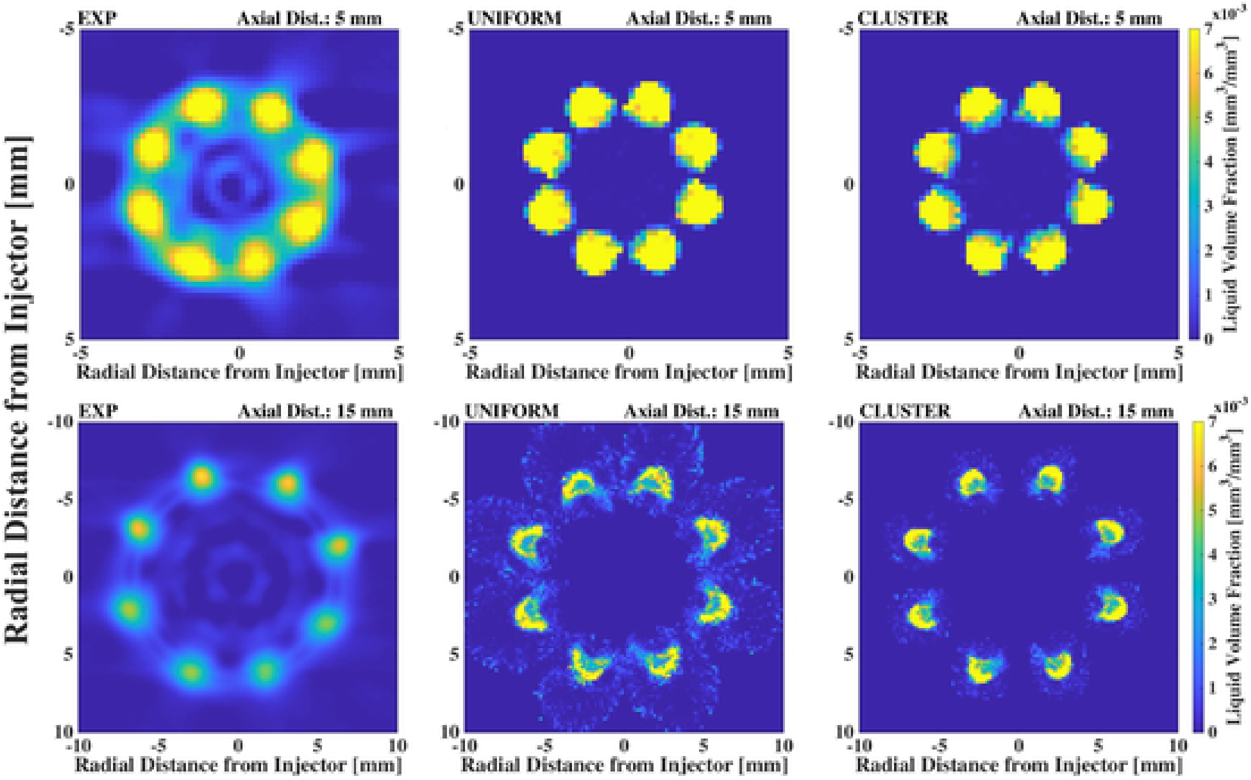

Fig. 9. LVF data for the Injector 1. Contrary to the X-ray data at Z = 2 mm, both parcel distributions predict higher LVF concentrations near the plume center. Also, both parcel distributions fail to predict the plume structure at an axial distance of 15 mm from the injector, highlighting the need for improved spray submodels.

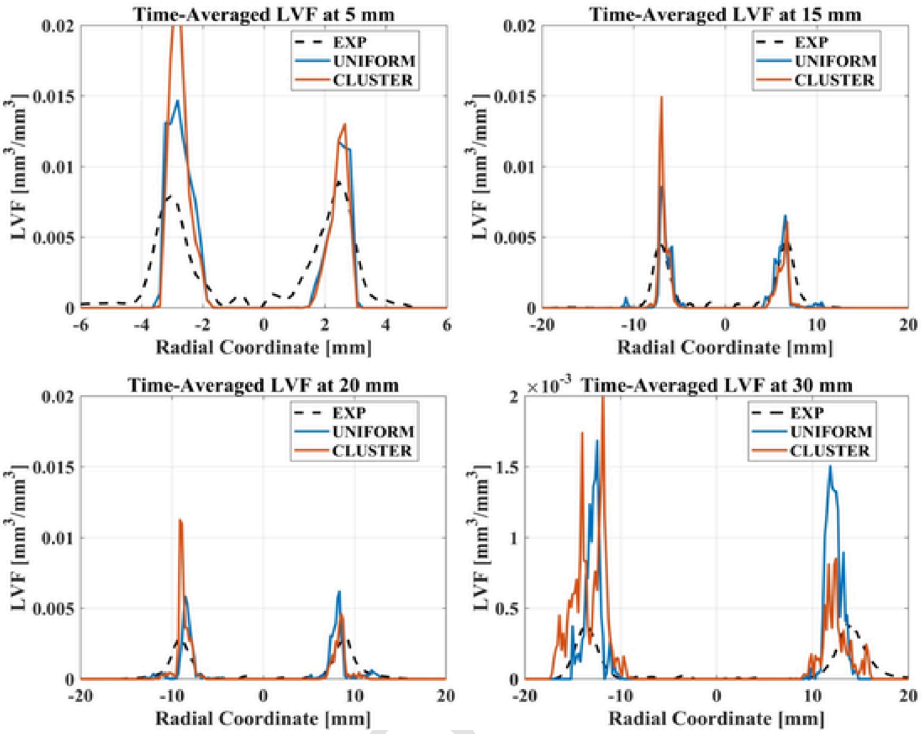

Fig. 10. Quantitative assessment of two opposed plumes from Fig. 9. The simulation using the “uniform” distribution consistently results in lower LVF than the one using the “cluster” distribution across all axial distances from the injector tip. Despite these differences and the overprediction of LVF from both simulation results, a decay in LVF with axial distance can be observed as in the experimental results.

ment, energy, and species transport. A modified Pressure Implicit with Splitting of Operator (PISO) method was employed for an iterative algorithm, and an additional Jacobi iteration for all quantities was performed to enforce strict conservation. A second-order central-differencing scheme was used for spatial discretization, and a first-order implicit Euler scheme was used for time advancement.

A simplified internal volume of the spray vessel and its computational grid configuration are shown in Fig. 2. Three FEs were used to provide a fine grid for the regions of interest: a cylindrical FE covering the near-nozzle region (red box in Fig. 2 (right)), an injector FE for each plume direction (green box), and a cylindrical FE for the downstream region (yellow box). The AMR was activated by monitoring the subgrid scales of velocity (threshold: 0.1 m/s), temperature (2.5 K), and void fraction (0.001). This strategy resulted in grid sizes as small as 0.25 mm. This grid size was intentionally selected to ensure consistency with the grid size typically used in Reynolds-Average Navier Stokes (RANS) engine simulations performed by industry. Additionally, different meshing strategies were examined to assess the validity of the selected mesh strategy. Parts of the 0.5-mm FE region highlighted in Fig. 2 (right) were further refined to 0.25 mm by relying on larger FE regions and less active AMR. While the specific results of this refinement are not presented here, it was confirmed that the simulation results remained consistent.

Fuel injection started at 0.0 ms and the simulation ran for 1.5 ms with a variable timestep whose upper limit was 0.5 μs for both injectors. A 7-component fuel surrogate was developed specifically for the Co-Optima E30 fuel [33], and its species composition is listed in Table 2. It is worth noting that previous work had used a 6-component fuel surrogate [34], including n-pentane, *iso*-pentane, n-heptane, *iso*-octane, toluene, ethanol). However, this 6-component surrogate did not accurately replicate the distillation curve of E30 fuel, mainly due to the absence of heavy hydrocarbon species with high boiling temperatures. On the other hand, the 7-component fuel surrogate closely matched the physical properties of E30, encompassing aspects such as distillation curve, research and motor octane numbers, density, and lower heating value. The physical properties of the original E30 fuel and its 7-component surrogate are summarized in Table 3. The Spray G injector simulations employed pure *iso*-octane, same as the fuel used in the experiments, which is a well-characterized fluid. Readers are referred to references [23,24] for details on its physical properties.

This study used a Lagrangian discrete phase model in the RANS framework. The blob injection method was used [35] where the injection mass flow rate was based on the measured rate of injection profiles shown in Fig. 3. The Kelvin-Helmholtz and Rayleigh-Taylor (KH-RT) breakup models [36] were utilized to describe the primary and secondary breakup processes. The breakup length was set as zero in the RT breakup model, resulting in both the KH and RT breakup mechanisms acting in a competing fashion as soon as the spray parcels are introduced in the computational domain. A detailed explanation and schematics on the KH-RT breakup model formulation can be found in [32,37]. The O’Rourke [38], Corrected-Distortion (CD) [39,40] and Frössling [41] models were used to compute turbulent dispersion, drop drag and mass/heat transfer between the liquid droplets and surrounding gas, and evaporation, respectively. The CD model was selected instead of the standard dynamic drop drag model since it accounts for the nonlinear deformation and oscillation experienced by droplets when injected into high-pressure, high-temperature conditions. A fundamental characteristic of DI injector designs is an inclusion angle smaller than the drill angle; thus, the spray inclusion angle for the Injector 1 was calibrated to 24° to enhance spray plume alignment. Similarly, the Spray G injector spray inclusion angle was set to 34° to improve model predictions [23]. Additionally, the spray cone angle followed a time-varying profile for the Injector 1, starting at 25° and linearly decreasing to 22° within 0.15 ms [42]. For the Spray G injector, a 20° cone angle was used as recommended in prior work [23].

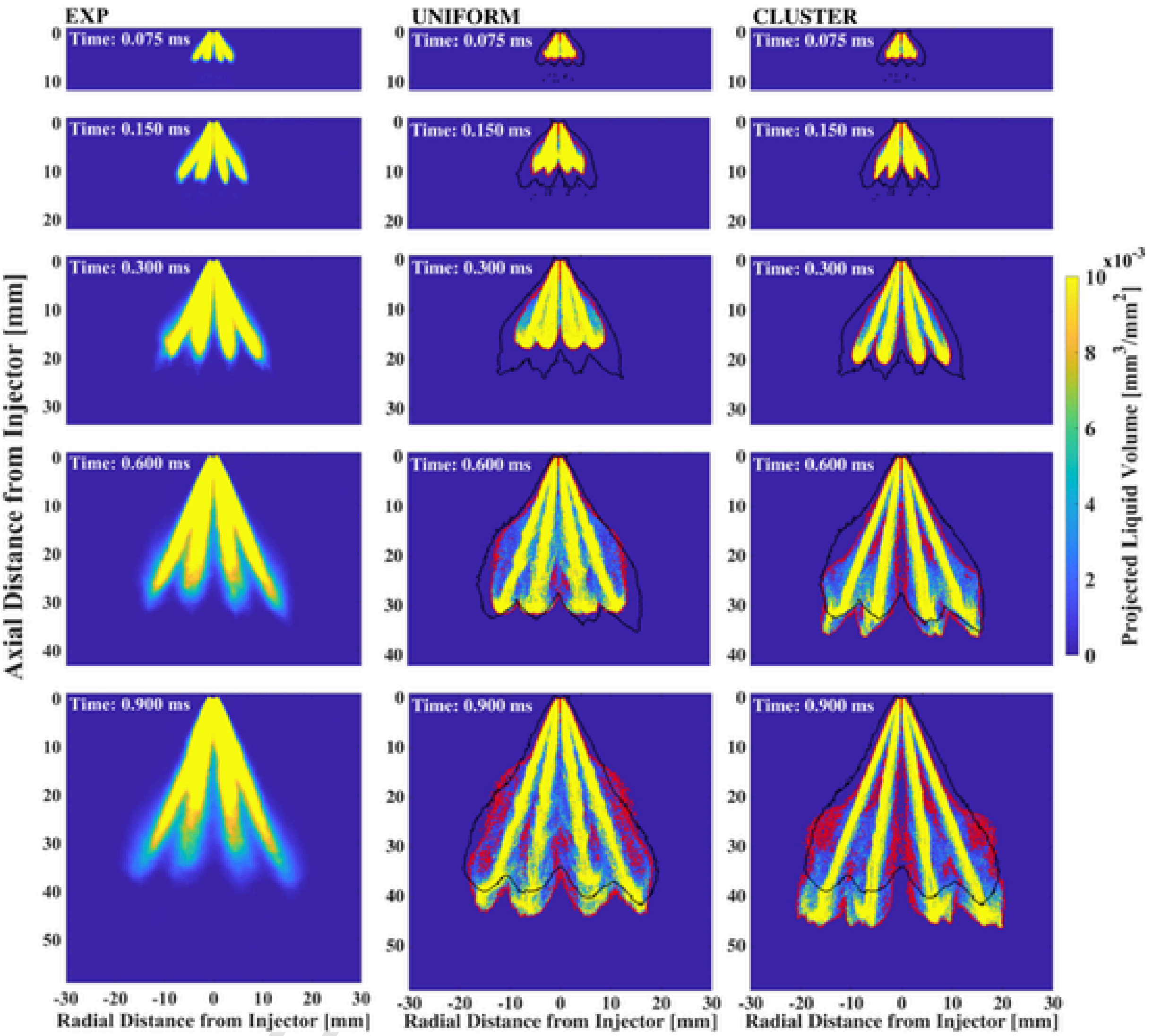

Fig. 11. Temporal evolution of PLV for the experimental data (left), "uniform" (middle), and "cluster" (right) distributions. The parcel distribution selection has a clear effect on the spray morphology due to the different axial droplet velocities. The increased droplet axial velocities results in longer LPL and more radial spreading of the spray plumes.

To evaluate the sensitivity of the spray simulation results to the choice of spray submodels and calibration and attain the best practices of physical-numerical submodels, various spray submodels were thoroughly evaluated regarding their impacts on liquid spray characteristics. This involved evaluating parcel distributions, droplet collision and collision outcome, and spray breakup model constants to understand their effects on spray morphology and improve agreement with measured liquid spray characteristics.

Concurrently, two different k-ε turbulence models, namely the Standard [43] and Re-Normalization Group (RNG) [44] models, were evaluated. For the sake of brevity, this paper primarily focuses on the comprehensive evaluation of spray submodels. The detailed assessment of turbulence models, including the comparison of Standard k-ε and RNG k-ε models, along with their respective impacts, is available in the appendix section ("*Effects of Turbulence Models and Initial Turbulent Flow Properties*") for those seeking an in-depth analysis. It is important to note that the spray submodel evaluations were conducted under the RNG k-ε model. Additionally, a sensitivity analysis of the droplet heat transfer coefficient scaling factor on spray characteristics was conducted. This analysis is particularly relevant as accurate prediction of the droplet evaporation process is essential for the future study of fuel-film prediction upon spray impingement, especially for multi-component fuels operating under cold conditions. The detailed results of this analysis are provided in the appendix section of "*Effect of Droplet Heat Transfer Coefficient*".

Table 4 lists the baseline setup and the investigated ranges for various models or constants. Each submodel was individually evaluated to isolate its effect, with the "Baseline" calibration (as shown in Table 4) serving as the common starting point unless otherwise specified.

3.1. *Metrics for CFD submodels validation*

As previously mentioned, this study utilized measured PLV, LVF, and fuel density distribution data to validate simulation results. Fig. 4 presents an example of a PLV contour selected from the simulation results. The liquid boundary was determined using a PLV threshold of $0.2{\cdot}10^{-3}$ mm^3 (liquid)/mm^2, following the ECN's recommendation [20, 23]. Various metrics were computed to validate CFD submodels against the experimental data, such as the liquid penetration length (LPL), liquid spray full widths (LFW) at 5 mm, 15 mm, and 25 mm downstream

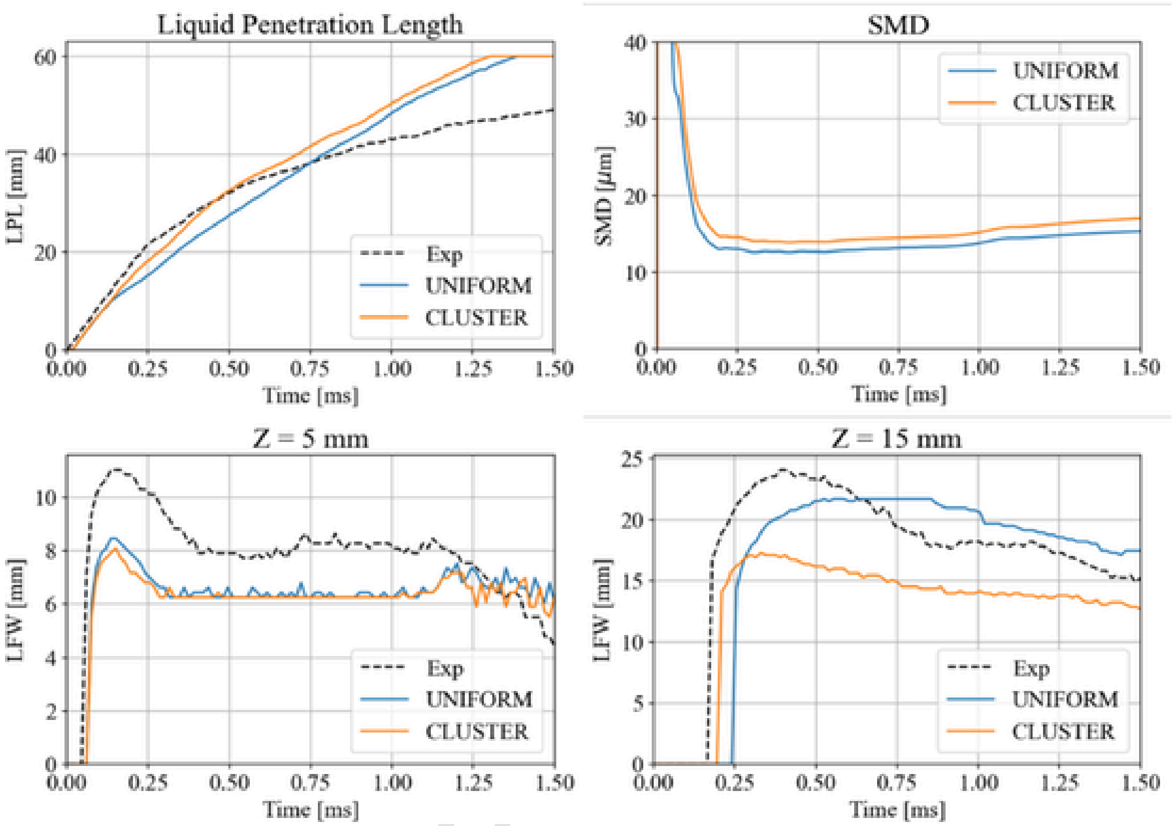

Fig. 12. LPL (top left), SMD (top right), LFW at Z = 5 (bottom left), and Z = 15 mm (bottom right). The “cluster” distribution results in longer LPL and smaller LFW at Z = 15 mm. However, the parcel distributions weakly affect the SMD (breakup) and LFW at Z = 5 mm.

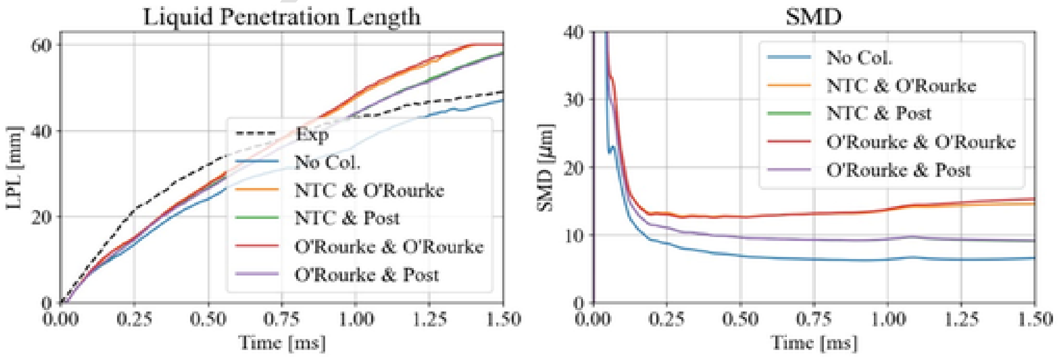

Fig. 13. LPL (left) and SMD (right) results from the evaluations of droplet collision and outcome models. Results clearly show a strong influence of droplet collisions on the spray's LPL and SMD. The collision outcome models also significantly impacted the spray behavior more than the collision models.

of the injector tip, and the shape of the liquid boundary in comparison to experimental results (black isoline). In Fig. 4, the LPL is defined as the furthest axial distance from the injector tip where the PLV exceeds the threshold of $0.2 \cdot 10^{-3}$ mm^3 (liquid)/mm^2. Similarly, the LFW is defined as the furthest radial distance between two points where the PLV exceeds the same threshold.

Additionally, radial LVF at axial distances of 5, 15, 20, and 30 mm were used to evaluate simulation results regarding plume alignment and structure. To examine the influence of parcel distribution on the spray plume structure, the radial fuel density distribution at an axial distance of 2 mm from the injector tip was analyzed. These radial profiles were shown in Fig. 1 for reference.

4. Results and discussions

4.1. *Effects of parcel distribution*

CONVERGE Computational Fluid Dynamics (CFD) offers two distinct numerical strategies for parcel distribution during injection: (1) the “uniform” distribution, which evenly spreads parcels throughout the spray plume, and (2) the “cluster” distribution, which concentrates parcels closer to the plume center. The difference between these distributions is related to how the axial component of the droplet velocity vector calculated, as elucidated below.

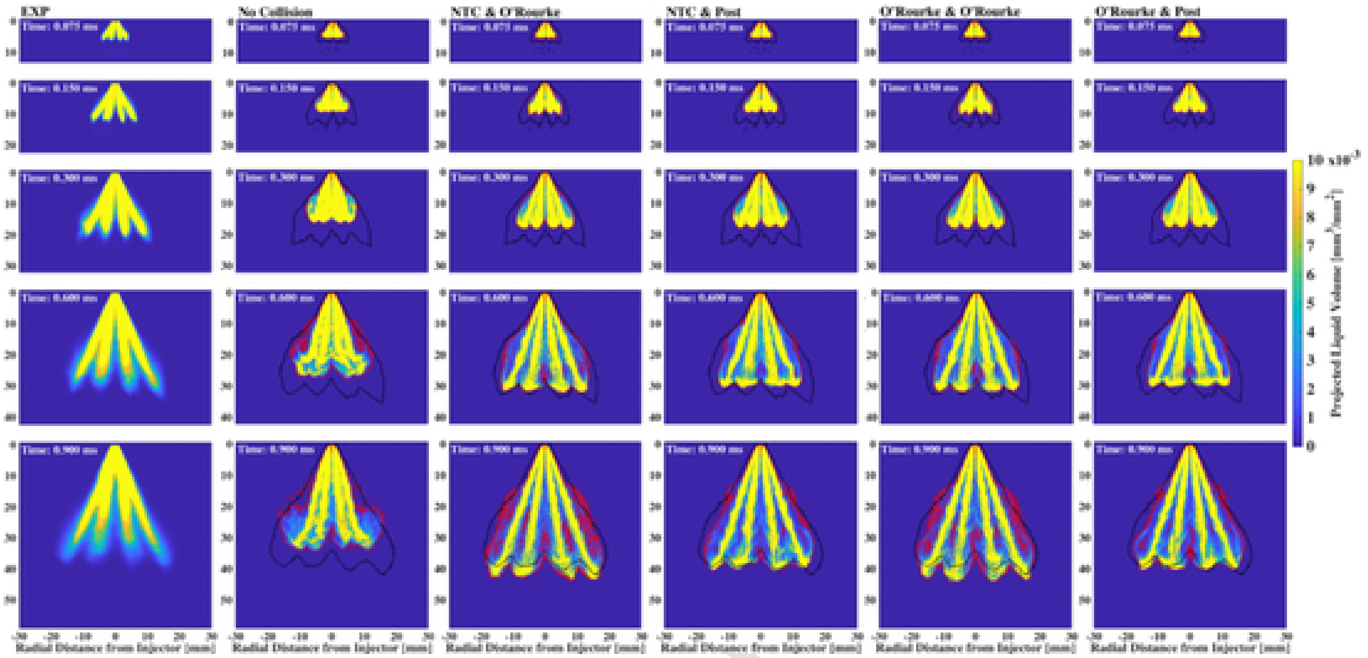

Fig. 14. Overall spray morphology is influenced by the collision model outcome choice. The Post collision outcome model results in smaller droplets, ultimately, leading to faster evaporation and narrower spray plumes.

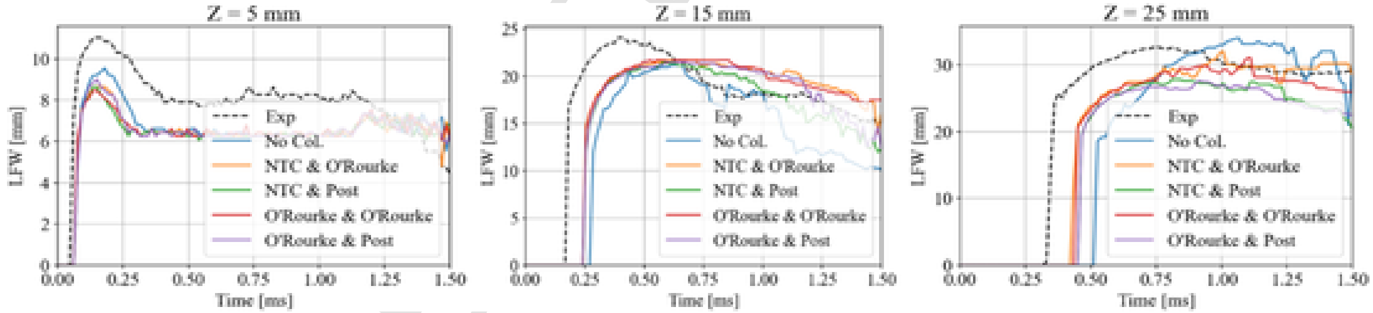

Fig. 15. LFW at axial distances of 5 (left), 15 (middle), and 25 mm (right) from the injector tip. Similar to LPL and SMD results, the LFW tends to be grouped by the collision outcome models, except at an axial distance of 5 mm where neither the droplet collision nor the outcome models affect the results.

To calculate the droplet velocity vectors during injection into the computational domain, CONVERGE employs two angles: the azimuthal angle, which governs the radial components of the droplet velocity vector and remains unaffected by the parcel distribution choices, and the off-axis angle, which defines the axial component of the droplet velocity vector. The off-axis angle determines the alignment of parcels with the nozzle's axis and is, therefore, altered based on the chosen parcel distribution. Fig. 5 illustrates the definition of these angles. Equations (2), (3)-(6), and (7) are used to calculate the axial component of the droplet velocity and the off-axis angle multiplier for both the "uniform" and "cluster" distributions.

$$U_{axial} = U_{local} * \cos(\theta * \alpha) \tag{2}$$

"Uniform"	"Cluster"
$\alpha_i = abs\,(random - 0.5)$(3) $\alpha_{ii} = 2 * (0.5 - \alpha_i)$(4) $\alpha_{iii} = \sqrt{\alpha_{ii}}$(5)	$\alpha = abs\,(random - 0.5)$ (7)
$\alpha = 0.5 * \alpha_{iii}$(6)	

These equations include several variables: U_{axial} which represents the axial component of the droplet velocity vector, U_{local}, denoting the local velocity, θ, representing the spray cone angle, and α, which is the off-axis angle multiplier. Both parcel distributions use the off-axis angle, which results from multiplying the cone angle by a random number between 0 and 0.5, represented by the off-axis angle multiplier. The key distinction lies in the weighting given to larger values in the "uniform" distribution through the square root in Equation (5). By favoring larger α values in the "uniform" distribution, the parcels are distributed across a larger area, as larger angles correspond to larger cone cross-sectional areas, thus decreasing the concentration near the plume center. In contrast, the equal weight for α values in the "cluster" distribution results in parcels distributed across a smaller area near the plume center. Fig. 6 presents this difference using the probability density functions (PDF) for α in the "uniform" and "cluster" distributions, showcasing the vary-

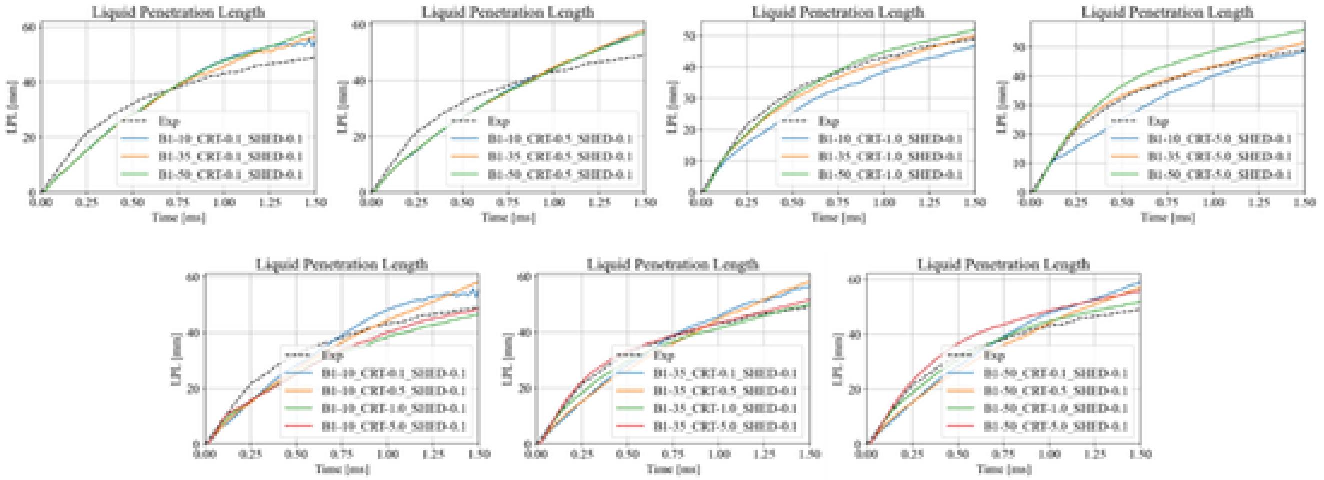

Fig. 16. Influence of the B_1 (top) and C_{RT} (bottom) constants on the LPL. As expected, increasing either constant delays breakup and increases the LPL. The results indicate that the influence of the B_1 constant increases as the C_{RT} constant value is increased. However, the converse is not true.

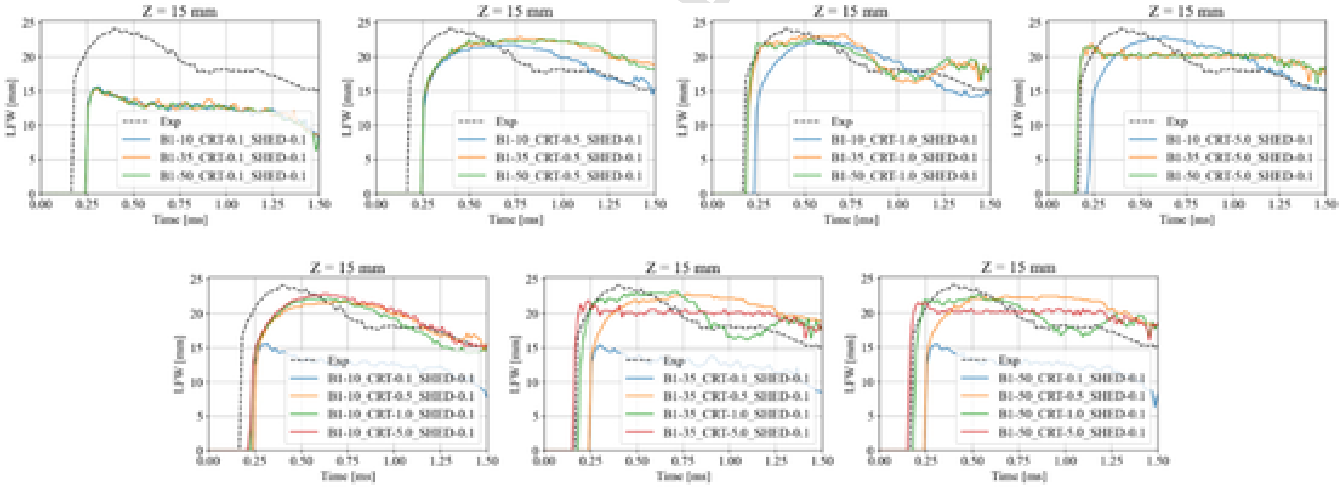

Fig. 17. The C_{RT} constant clearly has a strong influence on the LFW at 15 mm from the injector. In contrast, the B_1 constant has a minor effect on the LFW.

ing weighting of larger α values in the "uniform" distribution and the more even distribution of α values in the "cluster" distribution.

As indicated by Equations (2)-(7), the choice of parcel distribution has a significant impact on the axial component of the droplet velocity, thereby potentially influencing parameters such as the liquid penetration length and overall spray morphology. To assess this impact, CFD simulations were conducted for two experimental datasets, using identical baseline calibrations but employing different parcel distribution strategies. The goal was to evaluate the sensitivity of the spray simulation results to parcel distribution strategies. This investigation is divided into three regions of interest: (1) the near-field, encompassing axial distances up to 5 mm from the injector tip; (2) the mid-field, spanning axial distances between 15 and 20 mm; and (3) the far-field, denoting axial distances of 30 mm and beyond.

To maintain accuracy in the dense liquid region of the near field, fuel mass per unit volume data obtained from X-ray radiography is primarily utilized for near-field analysis, while the mid- and far-field regions reply on PLV and LVF datasets obtained from DBI experiments. Fig. 7 shows the results of the near-field analysis at an axial distance of 2 mm from the injector tip. These results are time averaged during the quasi-steady state portion of the injection, i.e., between 0.40–0.65 ms aSOI. The experimental data exhibit a discernible fuel mass concentration toward the center of plumes. Correspondingly, the simulation results show an increased fuel mass near the plume center in the "cluster" distribution case. Conversely, the "uniform" distribution yields a more uniform dispersion of fuel mass, aligning with expectations. Fig. 8 illustrates the radial profiles of the fuel density for the left-most plume at $y = 0$ mm. Neither distribution achieves the same level of fuel mass near the plume center. Nonetheless, the "cluster" distribution demonstrates a better qualitative and quantitative agreement regarding the plume structure.

Fig. 9 shows LVF results for Injector 1. Qualitatively, the trends observed in Fig. 9 are consistent with those seen in Fig. 7, indicating an increased LVF concentration toward the center of the plumes in both experimental and simulation results. However, unlike the fuel mass per unit volume results, both simulation results indicate an elevated liquid concentration near the plume center. This is likely due to the influence of further axial distances where drag, evaporation, and droplet collisions affect the spray behavior. The results in Fig. 9 show that neither parcel distribution effectively predicts the plume structure in the mid- and far-field regions. This suggests that factors beyond parcel distribution significantly influence plume structure in regions distant from the

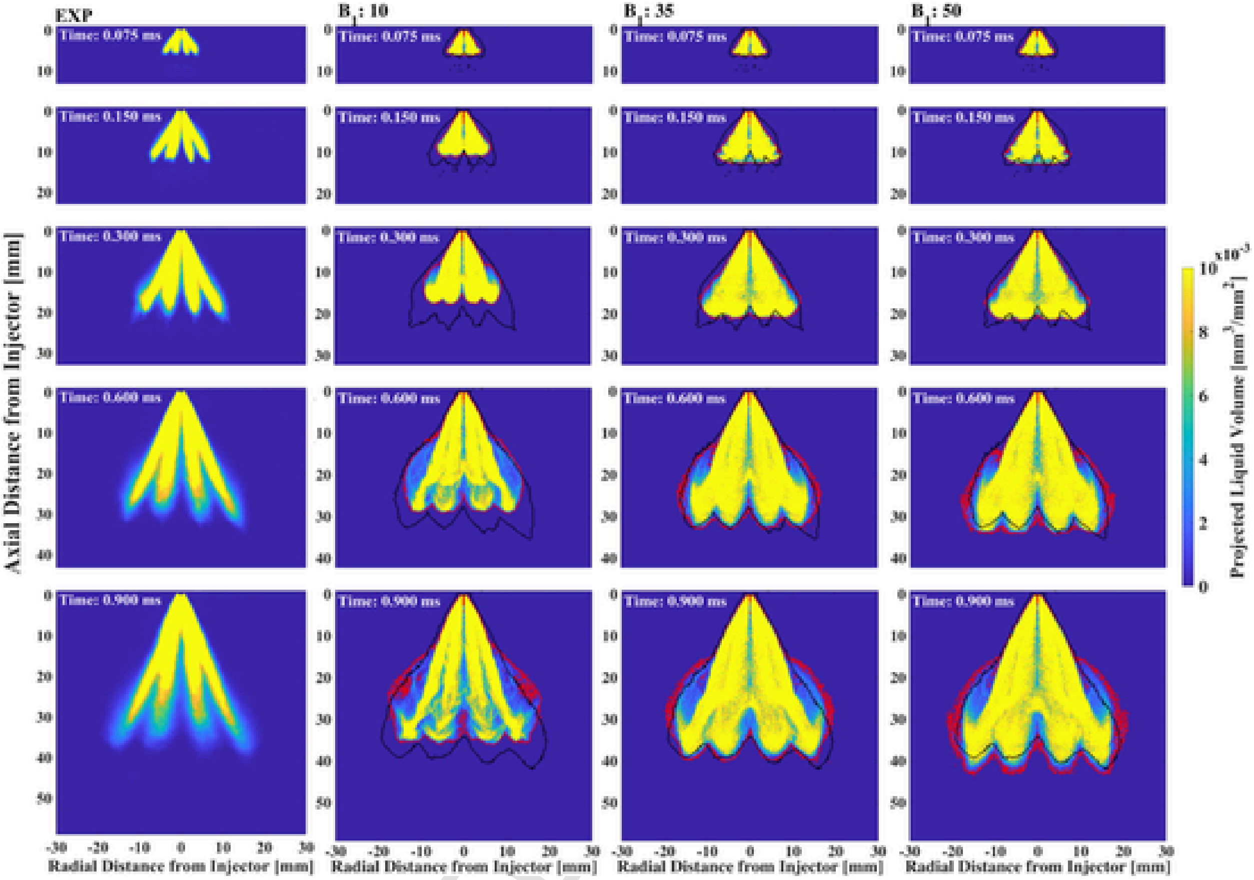

Fig. 18. Increasing the B_1 constant clearly results in breakup suppression indicated by the longer LPL and higher PLV. The influence of the B_1 constant in the plume diameters seems to be significant only for the lower values. The C_{RT} and shed factor constants were kept constant at 1.0 and 0.1, respectively.

injector. It is worth noting that the experimental data exhibit a more diffused nature, resulting from multiple injections and ensemble averaging, which differs from CFD outcomes based on a single injection without ensemble averaging.

Further quantitative assessments of LVF radial profiles for Injector 1, depicted in Fig. 10, reveal a contrasting trend in the near field compared to those in Fig. 8. The “uniform” distribution yields superior agreement with LVF experimental data, while the “cluster” distribution overpredicts LVF to a greater extent. Both distributions qualitatively capture the decay of LVF with axial distance, with the “cluster” distribution yielding higher overpredictions. Lastly, the total plume area is quantified at an axial distance of 5 mm for Injector 1 by applying an LVF threshold of $4{\cdot}10^{-3}$ mm^3 (liquid)/mm^3. The plume areas for experimental data, “uniform” distribution, and “cluster” distribution are 14.74 mm^2, 11.85 mm^2, and 9.68 mm^2, respectively. The “uniform” distribution underestimates the plume area by 19.6 %, whereas the “cluster” distribution overpredicts the plume are by 34.3 %. It’s important to emphasize that the accuracy of LVF data diminishes in regions with dense spray, such as those at an axial distance of 5 mm. Consequently, the quantitative comparisons serve to highlight trends rather than provide absolute accuracy. However, reliable calculation of bounding plume areas remains feasible for comparison with simulation outcomes.

Fig. 11 presents the temporal evolutions of the PLV in the X-Z plane and highlights the significant impact of the parcel distribution on spray morphology. The “cluster” distribution, which results in a higher axial component of the droplet velocity, causes droplets to concentrate in a smaller region of the gas field. This concentration leads to greater momentum transfer from liquid droplets to the gas phase, resulting in locally higher gas phase velocity and lower relative velocity between the gas and liquid phases. As a result, the drag acting on the liquid droplets is reduced, enabling deeper penetration into the chamber, and subsequently, a longer LPL, as shown in Fig. 11 and quantified in Fig. 12. This effect becomes more pronounced in the mid- and far-regions, explaining the similarity in LPL and LFW for both distributions in the near-nozzle region, as observed in Fig. 12. Additionally, owing to the alignment of the axial droplet velocity component with the orifice axis, the higher momentum in the “cluster” distribution leads to reduced plume-to-plume interaction, yielding larger droplet spreading and more distinct plumes. This phenomenon is also apparent in the LVF data in Fig. 9 (bottom row).

Fig. 12 further shows that the choice of parcel distribution only weakly affects the droplet breakup, as both distributions exhibit similar SMDs. However, there is a trend of slightly suppressed breakup in the “cluster” distribution due to the reduced drag forces, as discussed earlier. Moreover, the choice of parcel distribution weakly affects the spray LFW at Z = 5 mm in the near-nozzle region but strongly influences the LFW at Z = 15 mm.

Throughout this study, the authors observed a strong influence of the parcel distribution on spray morphology when parametrically varying the breakup model constants to improve quantitative agreement with LPL and LFW data. Using the “cluster” distribution, none of the breakup model constant combination matched the experimental data or replicated the spray morphology observed in the PLV data. However, a good agreement was achieved using the “uniform” distribution. For a more comprehensive evaluation of the effects of parcel distribution on the spray morphology and other spray submodels, more detailed discus-

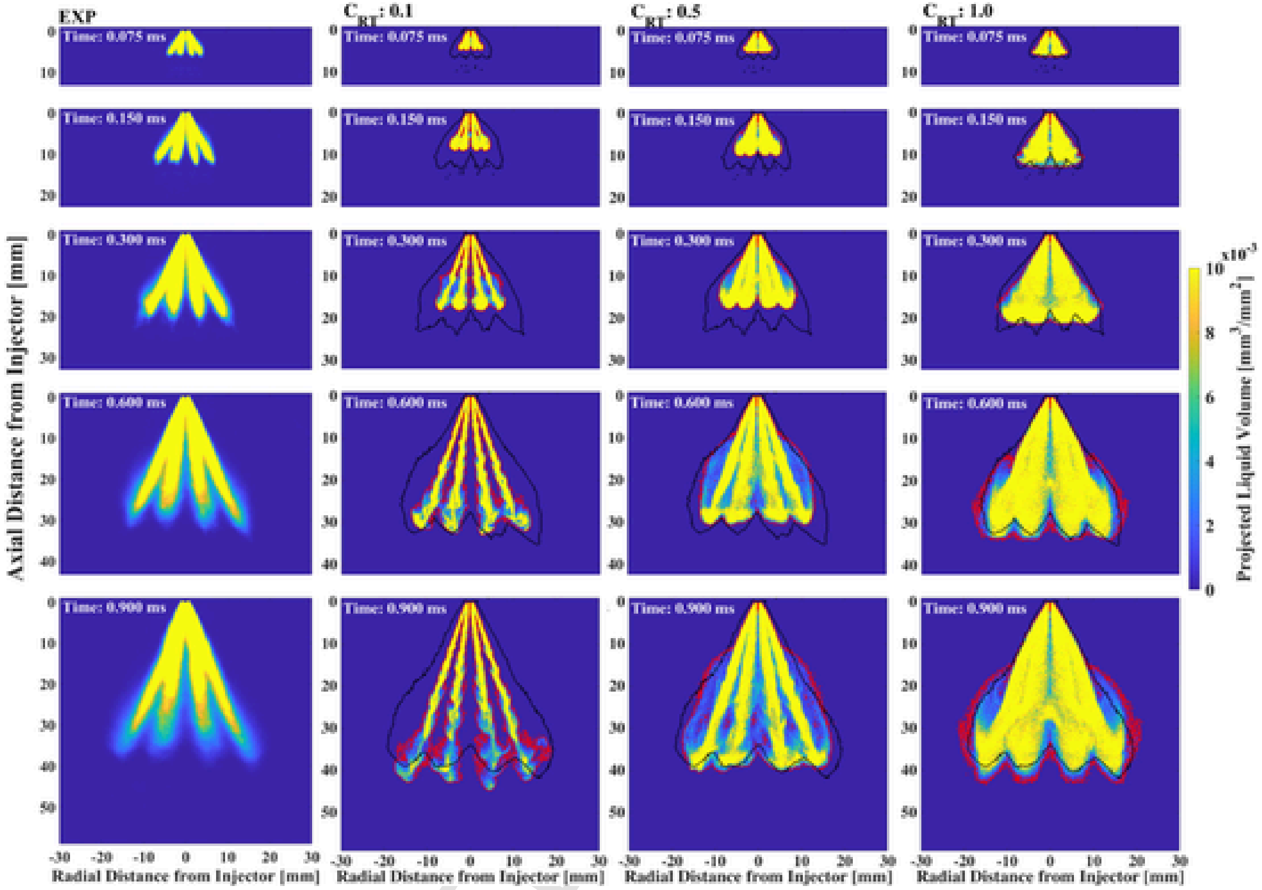

Fig. 19. Increasing the C_{RT} constant suppresses breakup, increasing the LPL and PLV. Notably, the C_{RT} had the strongest influence on the plume diameters. In these simulations, the B_1 and shed factor constants were kept at 50 and 0.1, respectively.

sions are presented in the appendix section of "*Effects of Breakup Model Constants using the "Cluster" Distribution*".

4.2. Effects of droplet collision and collision outcomes models

Droplet collisions are widely recognized for their significant influence on droplet size, which in turn affects droplet velocities, mixing, and overall spray morphology [38]. The outcome of a collision, whether it leads to bouncing, coalescence, or separation, plays a crucial role in shaping the spray characteristics [45]. Many existing collision models have been developed based on experimental observations of water droplets; however, studies have demonstrated that the collision behavior of hydrocarbon droplets may significantly differ from that of water droplets [46]. Therefore, to understand the influence of droplet collision and collision outcome models on the prediction of GDI spray behavior, particularly under cold-start conditions, available droplet collision and collision outcome submodels in CONVERGE were evaluated and compared against PLV experimental data from the Injector 1.

CONVERGE offers two droplet collision submodels: (1) O'Rourke [38] and (2) No-Time-Counter (NTC) [47]. Additionally, there are two collision outcome submodels: (1) O'Rourke [38] and (2) Post [45]. This study examined five combinations of these models: (1) no droplet collision, (2) NTC & O'Rourke, (3) NTC & Post, (4) O'Rourke & O'Rourke, and (5) O'Rourke & Post. In the cases accounting for droplet collisions, a collision mesh based on the concept of Hou [48] was used to decrease grid artifacts on the spray and improve computational efficiency. This collision mesh was five levels finer than the base grid size.

Fig. 13 shows the LPL and SMD for the five simulations. As it can be clearly seen, accounting for droplet collisions greatly affects both LPL and SMD, in agreement with previous findings [45,47]. These results demonstrated that inclusion of droplet collisions leads to increased LPL and SMD, likely due to the coalescence taking place after collisions. Fig. 13 also highlights an interesting trend that collision outcome submodels have a stronger influence on LPL and SMD compared to the collision submodels. This behavior can be explained by the consistent collision frequency calculations between the O'Rourke and NTC models, as also observed by Schmidt and Rutland [47]. On the other hand, the absence of separation after a collision in the O'Rourke model appears to result in larger droplets, as evidenced by the larger SMD values in Fig. 13 (right), causing the droplets to carry more momentum and ultimately increasing LPL, as seen in Fig. 13 (left). In terms of computational efficiency, the NTC model was slightly more cost-effective, with a 2.3% reduction in computational cost compared to the O'Rourke model, as its cost scales linearly with the number of parcels since only a subset of the parcels is used to represent the entire parcel population, while the O'Rourke model scales quadratically, evaluating the number of collisions with the entire parcel population [47]. A brief explanation of the differences between the two models is provided in appendix A.4. For a complete model formulation description, the interested reader is referred to references [38, 47].

Fig. 14 highlights the significant impact of droplet collision and collision outcome submodels on the overall spray morphology when analyzed through the PLV data. The coalescence resulting from droplet collisions causes an increase in SMD, allowing individual droplets to

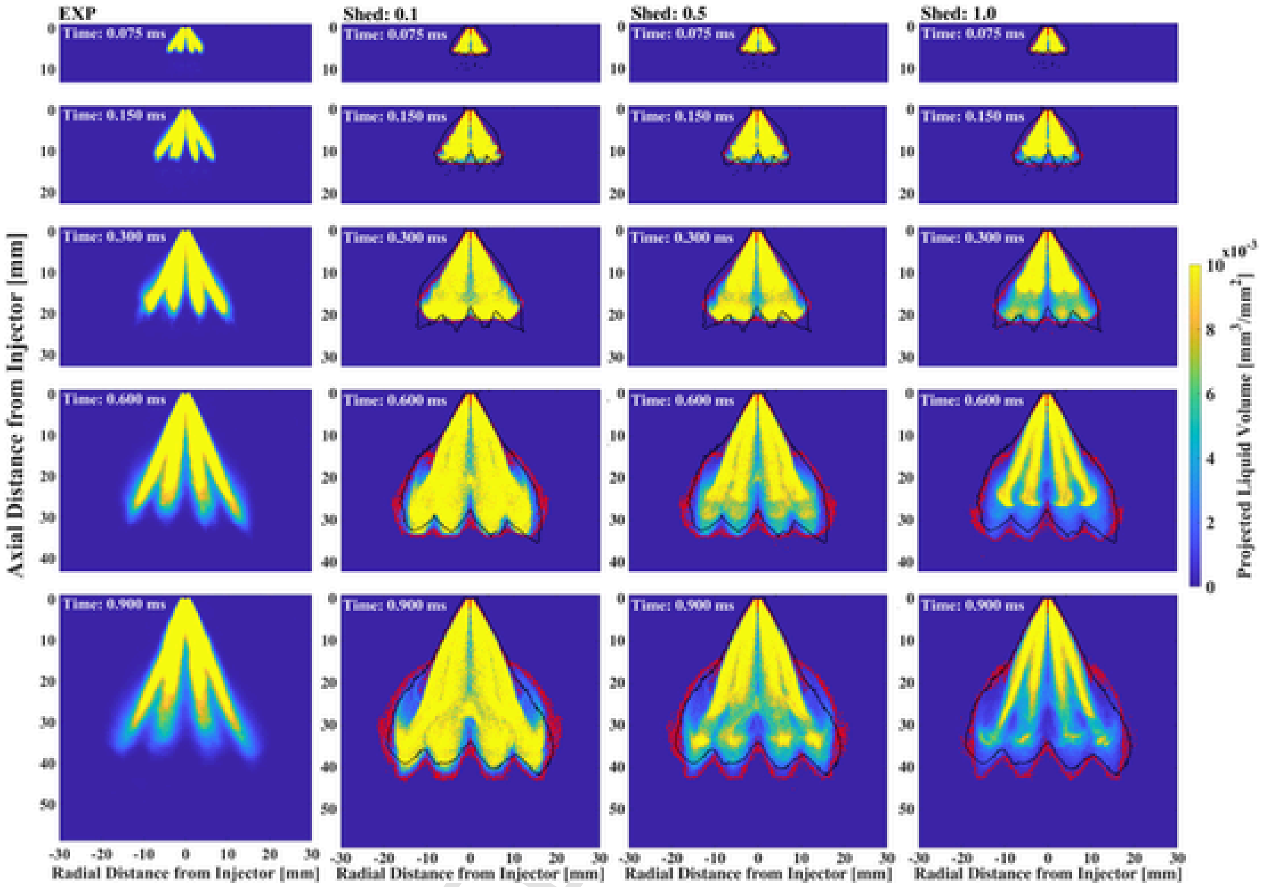

Fig. 20. By increasing the child droplet masses, through increasing the shed factor, the overall spray morphology is significantly improved, especially in terms of the axial PLV decay observed in the experimental results. This is a result of the overall reduced SMD brought about by the larger shed factor values. In these simulations, the B_1 and C_{RT} constants were kept at 50 and 1.0, respectively.

carry more momentum, which, in turn, leads to longer LPL and reduced plume-to-plume interaction. This reduced interaction results in more distinct plumes. Additionally, the pronounced difference in spray morphology when collisions are not considered highlights the necessity of accounting for collisions in GDI liquid spray simulations.

Fig. 14 showed a slightly wider liquid envelope for the simulations employing the O'Rourke outcome model. This trend is also evident in Fig. 15, where LFW results appear to group based on the collision outcome model in the mid- and far-field regions, i.e., orange and red lines are almost overlaying each other, specifically at axial distances of 15 and 25 mm from the injector, similar to the behavior observed in LPL and SMD. However, neither the droplet collision nor the outcome models significantly affect the results in the near-field region at an axial distance of 5 mm from the injector tip.

4.2.1. Effects of breakup model constants

The KH-RT breakup model has several model constants that control the breakup process. In this study, a parametric investigation focusing on the three key model constants, breakup time constant (B_1) and shed factor (s) within the KH model, as well as the breakup size constant (C_{RT}) within the RT model, was conducted. It is important to note that the RT breakup time constant (C_τ) was maintained constant across all cases following recommendations from previous studies [38,49]. According to the breakup model formulation, the breakup rate by the KH instabilities reduces with increased B_1 values. Higher shed factor values lead to the generation of larger child droplets, and increased C_{RT} values reduce the breakup of parent droplets into smaller child droplets via the RT instabilities. In the CONVERGE implementation, parcel breakup is first evaluated with the RT model; if this model cannot break up the parcel, then the KH model is responsible for breaking it up, assuming the relevant breakup timescale has been reached. The time constants of these models, i.e., B_1 and C_{RT}, are used to scale up or down the models' timescales, either promoting or suppressing the droplet breakup with either model; thus, there is a need to evaluate them thoroughly. As previously mentioned, the breakup length was set to zero in all simulations. In this parametric study, each model constant was independently varied within the ranges presented in Table 4, resulting in a total of 48 cases.

Fig. 16 shows the results of varying the B_1 (top row) and C_{RT} (bottom row) constants. The results clearly show that both model constants affect the LPL at all stages of the injection. Fig. 16 also shows that the effect of B_1 constant on simulation results is dependent on the C_{RT} values, where smaller C_{RT} values tend to mitigate the influence of B_1 due to a substantial increase in breakup rates driven by the RT instabilities. Although the B_1 constant does influence the effect of the C_{RT} constant, the latter's influence on the former is more pronounced. It is worth noting that for those aiming to achieve a good agreement in terms of LPL, Fig. 16 shows that multiple combinations of B_1/C_{RT} can yield satisfactory results. However, focusing only on one-dimensional metrics such as LPL can lead to significant mispredictions on the overall spray morphology, which will be further discussed below.

Fig. 17 shows the impacts of the B_1 and C_{RT} constants on the LFW at an axial distance (Z) of 15 mm. Notably, the C_{RT} constant has a substantial impact on the LFW (bottom row). As C_{RT} values increase, indicating a suppression of breakup by the RT instabilities, the LFW also

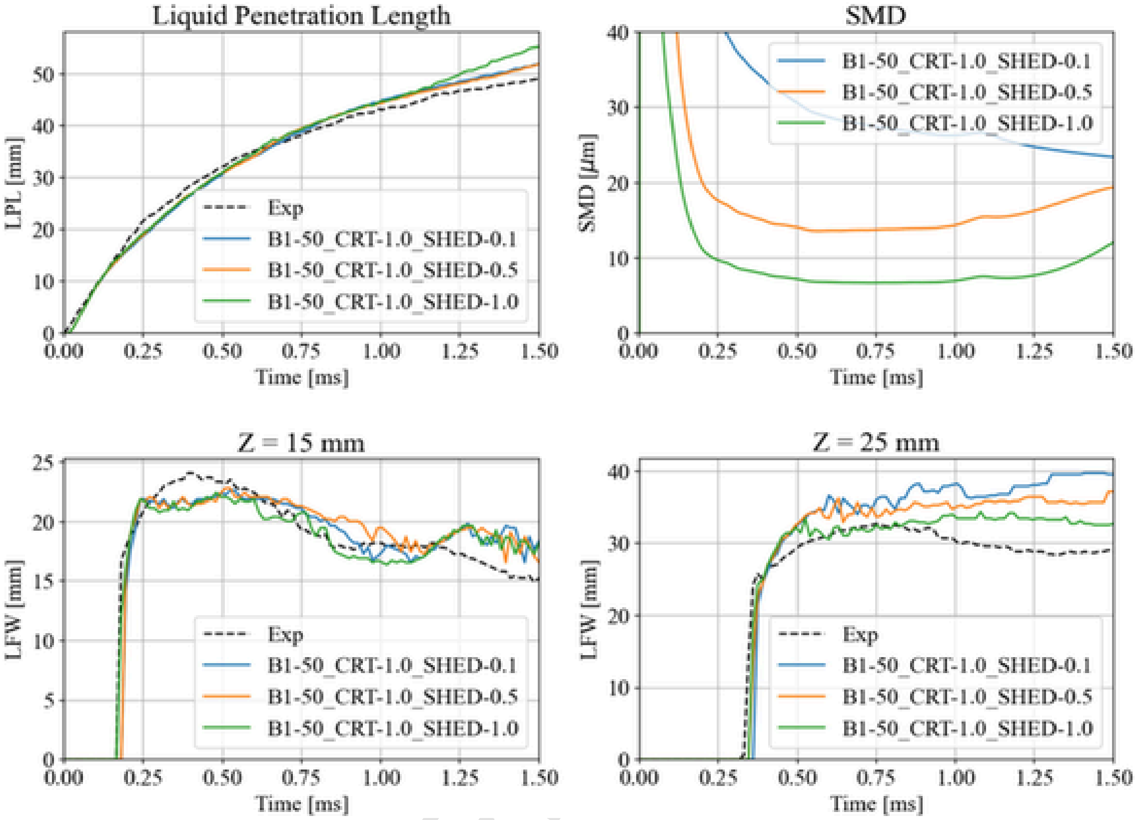

Fig. 21. Impact of the shed factor on the LPL, SMD, and LFW. A minimum impact was observed in the LPL and LFW at axial distances below 15 mm. The overall decreased SMD confirms the hypothesis of removing more mass from the parent droplets, the overall droplet size is decreased, which facilitates evaporation.

increases. In contrast, the B_1 constant has a relatively minor effect on the LFW.

To further evaluate the influence of the B_1 and C_{RT} constants on the spray morphology, Fig. 18 and Fig. 19 show the temporal evolution of the PLV during sweeps of B_1 and C_{RT}, while keeping all other model constants unchanged. The increased PLV values clearly shows the suppressed breakup due to the increased B_1. This leads to the presence of larger droplets and reduced overall evaporation, consequently resulting in the longer LPL trends observed in Fig. 16. Fig. 19 confirms the influence of the C_{RT} constant on the LPL, consistent with the findings in Fig. 16, but it also reveals a much stronger influence of the C_{RT} constant on the LFW and the diameters of individual plume. An increasing C_{RT} value leads to the suppression of breakup and the formation of larger plumes characterized by larger PLV values. In all these results, a relatively good agreement in LPL was observed. However, it became evident that other metrics, such as LFW or PLV did not necessarily align with the experimental data, highlighting the importance of adopting a comprehensive approach when calibrating spray models to ensure that various aspects of the spray behavior are accurately represented.

Varying the B_1 and C_{RT} model constants has demonstrated the potential for achieving a good agreement regarding LPL and LFW, as evidenced in Fig. 16 and Fig. 17. However, the overall spray morphology, as observed in the PLV data, was not adequately reproduced by the simulations. Specifically, the simulated plumes failed to exhibit distinct characteristics beyond $z \sim 15$ mm, and there was no observable decrease in the PLV with increasing axial distance. While some distinctions in spray plume characteristics could be achieved through different on B_1/C_{RT} combination, the axial decay in PLV values is not reproduced.

In response to this challenge, the shed factor constant, s, which controls the mass of the new child droplets after KH breakup, was systematically varied to capture this behavior. The PLV results of this parametric study, shown in Fig. 20, shows that an increase in the child droplet's mass, resulting from modifications to the KH breakup through the shed factor, can reproduce the axial decay in PLV. The increased child droplet's mass reduces the parent droplet's mass, resulting in an overall reduction in SMD, as shown in Fig. 21. This smaller SMD leads to faster evaporation, especially in the far regions, reproducing the experimentally observed decay in PLV. As qualitatively observed in Fig. 20, Fig. 21 shows the shed factor has a negligible impact on the LPL and LFW at $z = 15$ mm, although it has significant effect on LFW at $z = 25$ mm.

Finally, Fig. 22 provides insights into the impact of sweeping the B_1, C_{RT}, and shed factor constants on the LVF at an axial distance of 5 mm. As observed in the LFW plots at the same axial distance, the B_1 and shed factor constants shows a negligible effect on the LFW. This lack of impact also extends to the plume structures shown in Fig. 22. The plume diameters show minimal changes due to variations in the B_1 and shed factor constants, explaining the small effect of these variables on the LFW. In contrast, the C_{RT} constant strongly impacts the plume diameter and structure, thereby significantly affecting the LFW.

5. Improved spray model calibration

In this section, an enhanced calibration for the spray model, outlining a set of best practices specifically tailored for Injector 1, is introduced. These refinements are based on insights gained from the preceding model evaluations. Table 5 provides a comparative overview of the baseline and improved submodel calibrations, as well as the rationale behind each selection.

To showcase the improved agreement achieved by the developed best practice for Injector 1, Fig. 23 shows the temporal evolution of the PLV obtained from both baseline and best practice simulations, com-

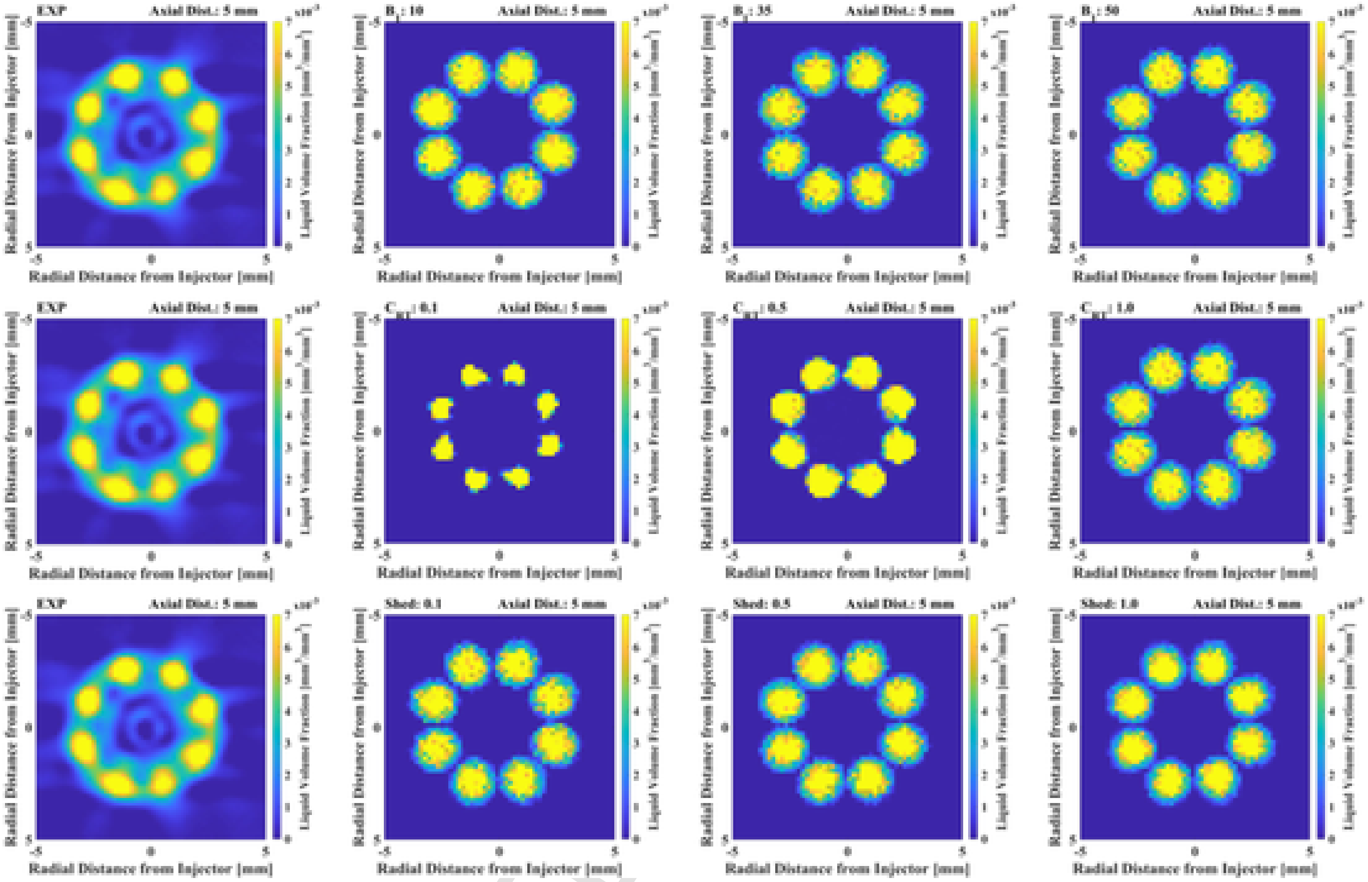

Fig. 22. Impact of the B_1, C_{RT}, and shed factor constants on the spray plume structure. The C_{RT} constant had the strongest effect on the LVF at $z = 5$ mm, being even more influential than the parcel distribution in altering the plume structure to achieve good agreement with experimental data.

pared to experimental PLV data. The LPL and LFW are notably better captured, and the axial decay in PLV is successfully reproduced – a behavior not achieved with the baseline calibration. In Fig. 24, the experimental, baseline, and best practice LVF results are presented from left to right. A significant improvement is observed in the near-field region, where a higher concentration of liquid is evident in the spray plumes, consistent the experimental observations. While the LVF is underpredicted at 15 mm, an improved LVF plume structure is achieved. Finally, Fig. 25 highlights the improved LPL and LFW achieved through the best practice calibration. The underprediction in the LPL is no longer observed, and the mismatch in LFW is reduced.

6. Conclusions

In this study, a systematic evaluation of spray submodels were conducted, leading to the development of a comprehensive set of best practices for physical-numerical submodels. These practices aims to facilitate accurate simulations of liquid spray behavior in a Direct-Injection Spark-Ignition (DISI) engine. This study represents a substantial stride and a necessary step toward the accurate prediction of fuel film evolution and soot formation in DISI engine performance during cold conditions. The main findings and recommendations are summarized as follows.

- Parcel distribution: The parcel distribution, which determines how droplets are distributed within the spray, was found to have a significant impact on the accuracy of spray model calibration. The “cluster” distribution provided improved results in the near field but overpredicted the Liquid Penetration Length (LPL) and failed to capture the spray morphology. In contrast, the “uniform” distribution provided better agreement with LPL, Liquid Full-Width (LFW), and spray morphology after a proper breakup model calibration.
- Droplet collision and collision outcomes model: Accounting for droplet collisions is crucial for capturing the spray morphology. The study highlighted that the collision outcomes model has a more significant influence than the collision model itself due to the different physics captured and the consistency in the frequency of collision calculations between the two models analyzed.
- KH-RT breakup model constants: The study evaluated the impact of the Kelvin-Helmholtz (KH) breakup model and the Rayleigh-Taylor (RT) breakup model constants on LPL, LFW, and spray morphology. It was found that the B_1 and C_{RT} constants strongly impacted LPL, while C_{RT} strongly impacted LFW and plume structure. The shed factor has a great impact on spray morphology, allowing the capture of axial decay in Projected Liquid Volume (PLV) typical of gasoline direct injection sprays.

In future work, the improved spray model setup developed in this study will be further evaluated using highly characterized ECN Spray G data across various thermodynamic conditions, fuels, and injector geometries. This extended evaluation will facilitate a more comprehensive analysis of parcel distribution trends and the influence of model constants under varying conditions. Furthermore, the established best practices will be incorporated into engine simulations to improve predictions of fuel film formation and soot emissions from DISI engines operating in cold conditions.

Table 5
Summary of baseline and best practices for spray model calibrations. The "Reason" column summarizes the rationale behind the choice of each sub-model or constant value.

Physics	Baseline	Best Practice	Reason
Turbulence Model	Standard k-ε	RNG k-ε	The spray model calibration is influenced by the turbulence model, necessitating consistency with the turbulence model employed in the engine simulation setup.
Injected Parcel Distribution	Uniform	Uniform	Having parcels uniformly distributed across the spray cone provided overall improved spray morphology, LPL, and LFW. LVF plume structure was effectively captured following breakup model calibration.
Droplet Collision Model	O'Rourke	NTC	Physically, both models estimate comparable collision frequencies with the computational cost of the NTC model scaling linearly with the number of parcels, as opposed to the quadratic scaling in the O'Rourke model.
Droplet Collision Outcome Model	O'Rourke	Post	In addition to the grazing collisions and coalescence, the Post model accounts for droplet separations (stretching and reflexive), leading to improved predictions for LPL.
KH breakup: B_1 constant	5.0	50	Increasing this constant results in delayed droplet breakup. In this work, it improved agreement in spray morphology, LPL, and LFW.
KH breakup: Shed Factor	0.1	1.0	Increasing this constant results in larger droplets after the KH breakup. This improved spray morphology and allowed the prediction of the axial decay in PLV.
RT breakup: C_{RT}	0.6	1.0	Increasing this constant results in delayed droplet breakup. In this work, it improved agreement in spray morphology, LPL, and LFW.
Droplet HTC Scaling	1.0	1.0	Increasing this scaling factor will lead to faster droplet evaporation. In this work, enhanced LPL could be achieved with a 5.0x multiplier at a slight compromise in the overall spray morphology. However, the use of this multiplier is only justified in the presence of uncertainties in the fuel (surrogate) physical properties.

CRediT authorship contribution statement

Diego Bestel: Writing – original draft, Visualization, Validation, Methodology, Investigation, Formal analysis, Conceptualization. **Joohan Kim:** Visualization, Methodology, Investigation, Formal analysis. **Le Zhao:** Writing – review & editing, Supervision, Project administration, Funding acquisition. **Anqi Zhang:** Supervision. **Ji-Woong Park:** Supervision. **Fabien Tagliante:** Methodology, Data curation. **Lyle Pickett:** Methodology, Data curation. **Muhsin Ameen:** Writing – review & editing, Supervision, Project administration, Conceptualization. **Roberto Torelli:** Writing – review & editing, Supervision, Resources, Project administration, Methodology, Funding acquisition.

Declaration of competing interest

The authors declare that they have no known competing financial interests or personal relationships that could have appeared to influence the work reported in this paper.

Data availability

Data will be made available on request.

Acknowledgements

The submitted manuscript has been created by UChicago Argonne, LLC, Operator of Argonne National Laboratory (Argonne). Argonne, a U.S. Department of Energy (DOE) Office of Science laboratory, is operated under Contract No. DE-AC02-06CH11357. This article has also been co-authored by employees of National Technology & Engineering Solutions of Sandia, LLC under Contract No. DE-NA0003525 with the U.S. Department of Energy (DOE).

This paper describes objective technical results and analysis. Any subjective views or opinions that might be expressed in the paper do not necessarily represent the views of the U.S. Department of Energy or the United States Government. The U.S. Government retains for itself, and others acting on its behalf, a paid-up nonexclusive, irrevocable worldwide license in said article to reproduce, prepare derivative works, distribute copies to the public, and perform publicly and display publicly, by or on behalf of the Government. DOE will provide public access to these results of federally sponsored research in accordance with the DOE Public Access Plan https://www.energy.gov/downloads/doe-public-access-plan.

This work is part of a larger effort known as the *Initiative for Modeling Propulsion And Carbon-neutral Transportation* (IMPACT) Consortium. The authors wish to thank:

1. Aramco Research Center – Detroit for funding the study.
2. Bebop High Performance LCRC cluster at Argonne National Laboratory.
3. Convergent Science Inc., for providing the CONVERGE CFD software licenses.

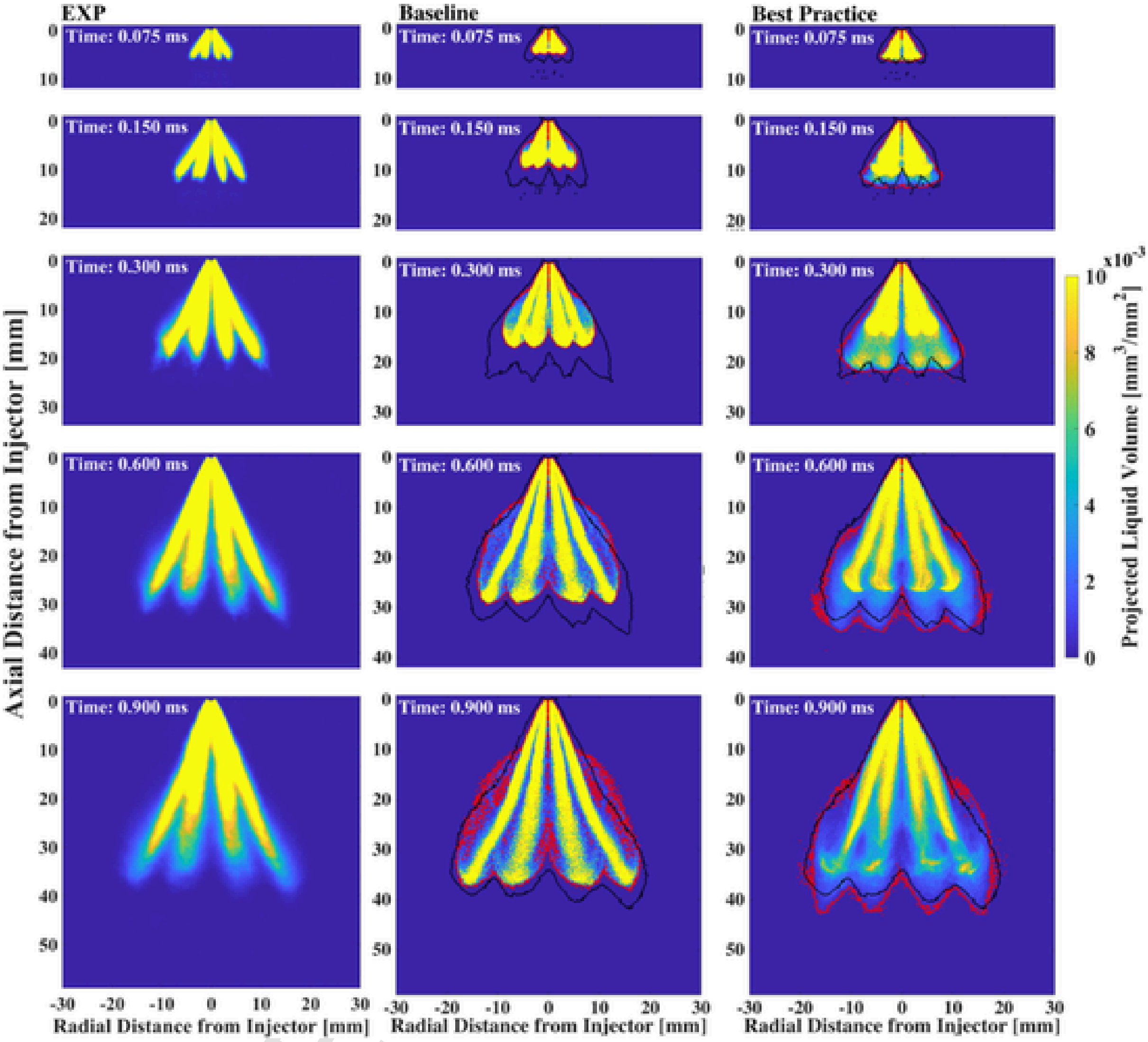

Fig. 23. Temporal PLV evolution of the experimental (left), baseline (center), and best practices (right) results. Spray morphology, LPL, and LFW are significantly improved with the developed best practice calibration.

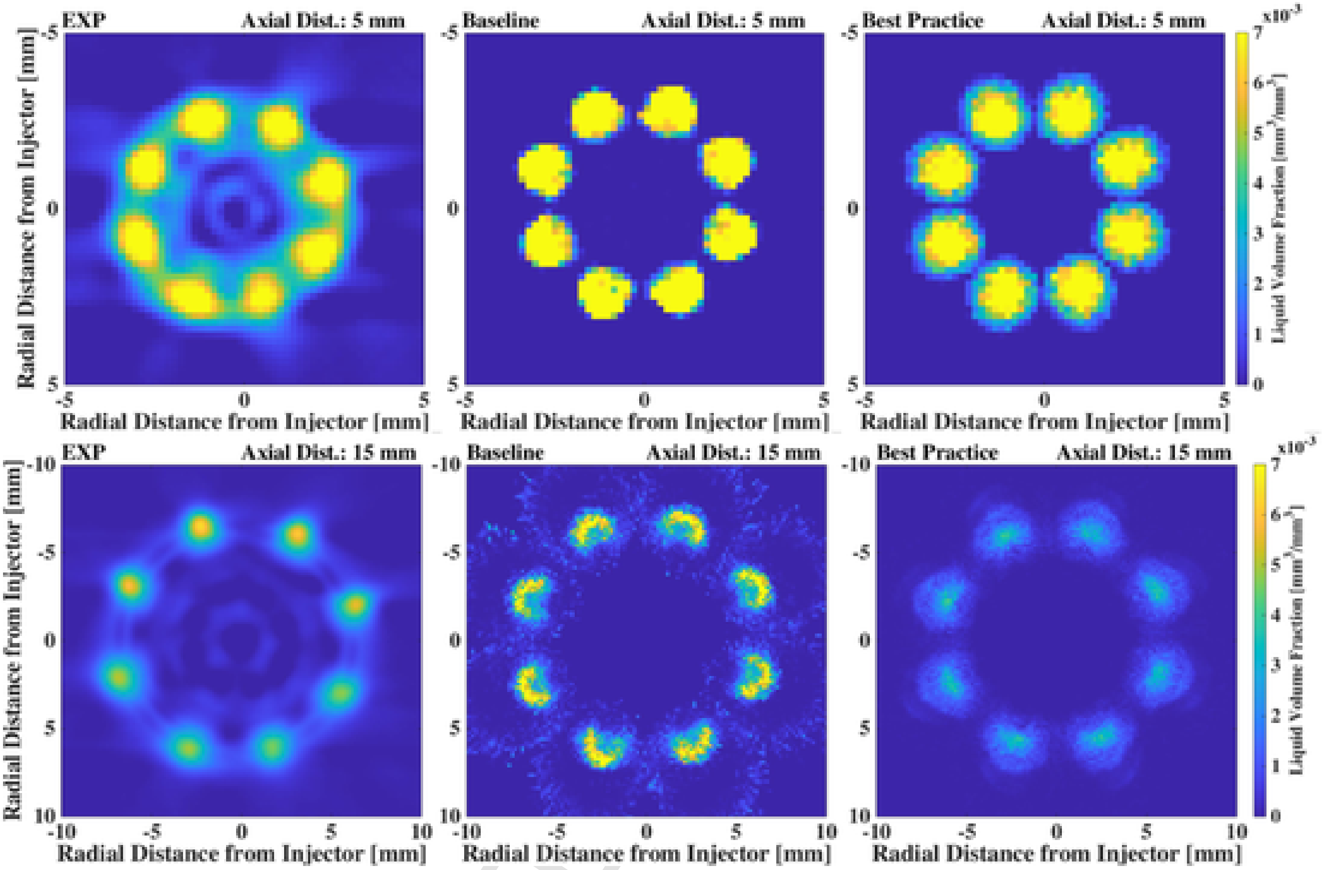

Fig. 24. The LVF plume structure exhibits notable enhancement through the developed best practice calibration, even in the near-field region with the "uniform" parcel distribution.

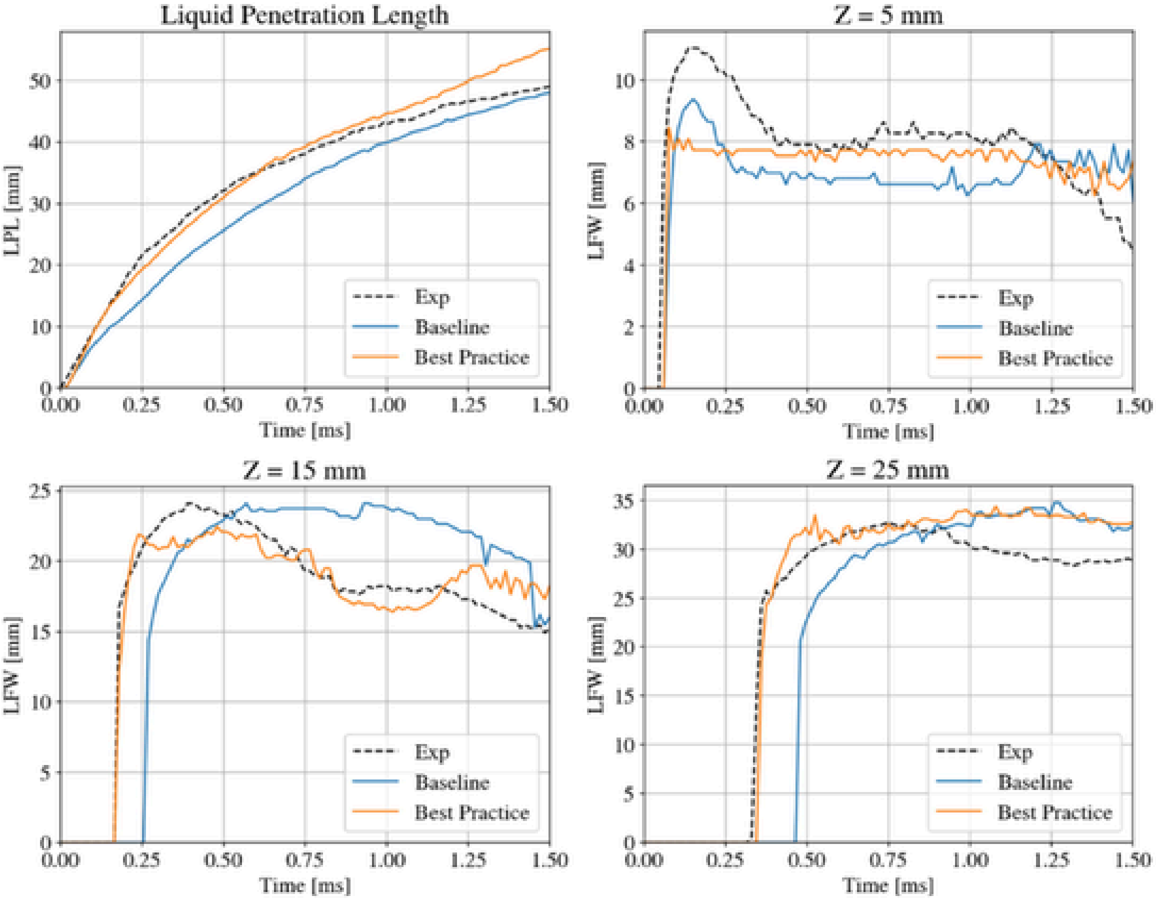

Fig. 25. The LPL and LFW are well captured by the best practice calibration. The late overprediction in LPL can be improved by increasing the heat transfer coefficient scaling but at the expense of overall spray morphology.

A. Appendix

A.1. Effects of turbulence models and initial turbulent flow properties

Simulation of a free spray in a vessel usually employs the use of RANS Standard k-ε turbulence model for turbulence modeling. However, when transitioning from vessel simulations to engine simulations, it is recommended to switch to the RNG k-ε model. The RNG k-ε model, derived from the dynamic renormalization group method and free of case-specific constants [44], has become the standard for modeling turbulent flows in internal combustion engines. This transition poses a potential risk as the model calibration from the spray-matching study may not hold when switching turbulence models. Hence, it is worth examining the performance of both turbulence models in simulating free spray in the vessel and ensure that the macroscopic liquid spray structure remains consistent.

When utilizing a RANS turbulence model, defining the initial condition for turbulent kinetic energy (k) and eddy dissipation rate (ε) is crucial. In this study, the initial conditions of k and ε were adopted from the ECN Spray G data [23]. For ECN Spray G, the measured root-mean-square of turbulent velocity fluctuations (u') is $6.5\bullet10^{-2}$ m/s, and the ratio of the integral length scale (l_t) to domain characteristics length (l) is 1.53%. Using equations to calculate $k = 1.5u'^2$ and $\varepsilon = C_\mu^{0.75}k^{1.5}/l_t$, the initial conditions for turbulent flow properties are determined as $k = 6.4\bullet10^{-3}$ m^2/s^2 and $\varepsilon = 5.08\bullet10^{-2}$ m^2/s^3 (using a model constant $C_\mu = 0.09$ for the Standard k-ε model). It is worth noting that this initial condition was not measured in the constant-flow spray vessel used with Injector 1, so there are uncertainties in using the k and ε from the constant-volume vessel. In a case where no measured data is available, a set of default values ($k = 1$ m^2/s^2, $\varepsilon = 100$ m^2/s^3) is commonly employed based on recommendations from the CFD software developers. The significant disparity between the measured and recommended values necessitated a sensitivity analysis of the turbulent flow properties.

When the Standard k-ε model is employed for free-spray simulations, the turbulence model constant, $C_{\varepsilon1}$, is usually adjusted to match experimental data, such as liquid and vapor penetrations, a practice known as round-jet correction [50]. Previous studies have reported various values for $C_{\varepsilon1}$, including $C_{\varepsilon1} = 1.5$ for the diesel injector under ECN Spray A condition [51], $C_{\varepsilon1} = 1.5$ for the ECN Spray G injector and G1 condition [21], and $C_{\varepsilon1} = 1.55$ for the ECN Spray G injector and G3 condition [22], used as the round-jet correction for the Standard k-ε model. Therefore, the calibration of $C_{\varepsilon1}$ was a significant aspect of this study. A detailed discussion will be presented below.

Table 6
Investigated turbulence models and initial conditions for turbulent flow.

Turbulence Model	Measured (Spray G1) k_i/ε_i	Arbitrary k_i/ε_i
Standard *k*-*ε*	$k_i = 6.4 \cdot 10^{-3}$ m^2/s^2 $\varepsilon_i = 5.08 \cdot 10^{-2}$ m^2/s^3	$k_i = 1.0$ m^2/s^2 $\varepsilon_i = 100$ m^2/s^3
Standard *k*-*ε* with Round-Jet Correction	$k_i = 6.4 \cdot 10^{-3}$ m^2/s^2 $\varepsilon_i = 5.08 \cdot 10^{-2}$ m^2/s^3	$k_i = 1.0$ m^2/s^2 $\varepsilon_i = 100$ m^2/s^3
RNG *k*-*ε*	$k_i = 6.4 \cdot 10^{-3}$ m^2/s^2 $\varepsilon_i = 5.08 \cdot 10^{-2}$ m^2/s^3	$k_i = 1.0$ m^2/s^2 $\varepsilon_i = 100$ m^2/s^3

Figure 26 shows the PLV data from the simulation results using a colormap, with a black isocontour line denoting the experimental PLV boundary at a threshold of $0.2 \cdot 10^{-3}$ mm^3 (liquid)/mm^2. The top row shows the results for cases with an initial turbulent kinetic energy dissipation rate (ε_i) calculated based on the ECN Spray G1 data. The bottom row shows results for ε_i typical of initial conditions for engine simulations. It is interesting to notice the non-negligible difference in the liquid spray behavior. Starting with the results for $\varepsilon_i = 5.08 \cdot 10^{-2}$ m^2/s^3 (top row), the Standard *k*-*ε* model predicts a shorter liquid penetration at $t = 0.9$ ms after the start of injection (aSOI). Towards the end of the injection, it predicts the deflected outward spray plume, accompanied by a reduced liquid spray width in the midstream (e.g., $z = 20$ mm). This behavior is not consistent with the experimental data (shown on the left side of Figure 26). On the other hand, the Standard *k*-*ε* with the round-jet correction and RNG *k*-*ε* models maintain the original plume direction and exhibit an overall similar spray morphology. When ε_i is arbitrarily increased to 100 m^2/s^3 (bottom row), the plume deflection of the Standard *k*-*ε* becomes more pronounced, which aligns with prior studies that have used this correction to improve simulation results [21,22,51].

Conversely, the RNG *k*-*ε* model provided spray morphology similar to that observed with the lower ε_i. The reason for this insensitivity of the RNG *k*-*ε* to the initial conditions is due to the comparable production and destruction of *k* in the two cases, whereas the production and destruction of *k* significantly differ in the Standard *k*-*ε* model between the two conditions. This suggests that the primary source of turbulence generation and destruction in the RNG *k*-*ε* setup is the spray itself and not the quiescent environment, which is physically expected when injecting fuel into a quiescent vessel. These results highlight the significant influence of the initial turbulent flow conditions on the spray morphology predictions from the Standard *k*–*ε* model. The sensitivity to initial *ε* conditions and the choice of turbulence model indicates that a calibration developed using the Standard *k*-*ε* model may not be applicable to engine simulations, typically carried out using the RNG *k*-*ε* turbulence model. To ensure consistency between the vessel and engine simulations in future work and remove the influence of unknown initial conditions (k_i and ε_i) in experiments, the RNG *k*-*ε* model is selected for the vessel simulations moving forward.

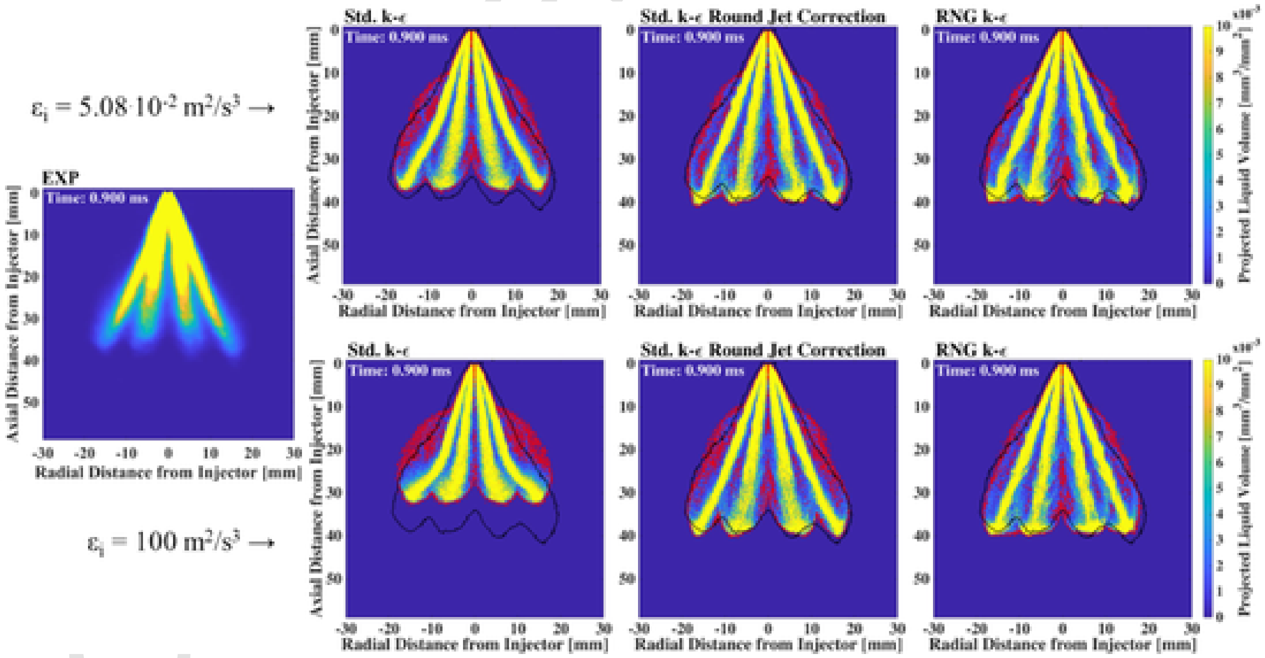

Fig. 26. Simulation results for the evaluated turbulence models and the two ε_i: $5.08 \cdot 10^{-2}$ m^2/s^3 (top row) and 100 m^2/s^3 (bottom row). Black isoline represents the experimental PLV contour. Simulation results clearly show that the Standard *k*-*ε* turbulence model is sensitive to ε_i. This implies that consistency needs to be maintained between vessel simulations used to generate the spray model calibrations and the engine simulations where the spray models are implemented.

A.2. Effects of breakup model constants using the "Cluster" distribution

Repeating the parametric study using the "cluster" distribution to evaluate the impact of parcel distribution on the spray morphology is a valuable step to gain a comprehensive understanding of the modeling approach. It is noteworthy that the same trends regarding the effects of the B_1 and C_{RT} constants observed with the "uniform" distribution were also observed with the "cluster" distribution. This consistency suggests that these constants have a consistent influence on the spray characteristics regardless of the parcel distribution. However, the shed factor was found to have a different impact when using the "cluster" distribution compare to the "uniform" distribution. In the case of "cluster" distribution, the shed factor did not seem to influence the spray morphology. Additionally, the axial decay in the PLV could not be reproduced with the "cluster" distribution.

These findings highlight the importance of considering both the parcel distribution and the specific breakup model constants in spray simulations. The choice of parcel distribution can significantly affect the results and should be carefully considered based on the specific goals of the simulation. The interaction between parcel distribution and model constants is complex, and the selection should be made with a clear understanding of the desired simulation outcomes. In some cases, the "uniform" distribution might provide better agreement with experimental data and overall spray morphology, as indicated in the study. This underscores the importance of conducting a thorough sensitivity analysis and calibration when setting up spray models for specific applications.

Figure 27 shows the PLV results for both the "uniform" distribution (center) and "cluster" distribution (right) when utilizing the best-performing breakup model calibrations for each distribution. These best performing calibrations were selected based on their agreement with LPL and LFW at $z = 5$, 15, and 25 mm. As can be seen, even for the best performing breakup model calibration, the "cluster" distribution yields a considerable overprediction in LPL, along with an inaccurate representation of the overall spray morphology, especially regarding the axial decay in PLV, a typical behavior of GDI sprays [28]. On the contrary, the "uniform" distribution exhibits a better agreement in terms of LPL, LFW, and the overall spray morphology.

Figure 28 shows the LVF at axial distances of 5 and 15 mm. Similarly to what was previously observed, both distributions show a higher liquid concentration near the plume center, with the "cluster" distribution showing a more pronounced concentration. In this near-field region, both best performing calibrations appear to capture the plume structure effectively, with total plume areas of 14.40 mm^2 and 10.66 mm^2 for the "uniform" and "cluster," respectively. The underprediction in plume area is essentially mitigated using the "uniform" distribution with an appropriately calibrated breakup model, an outcome that was unattainable with the "cluster" distribution.

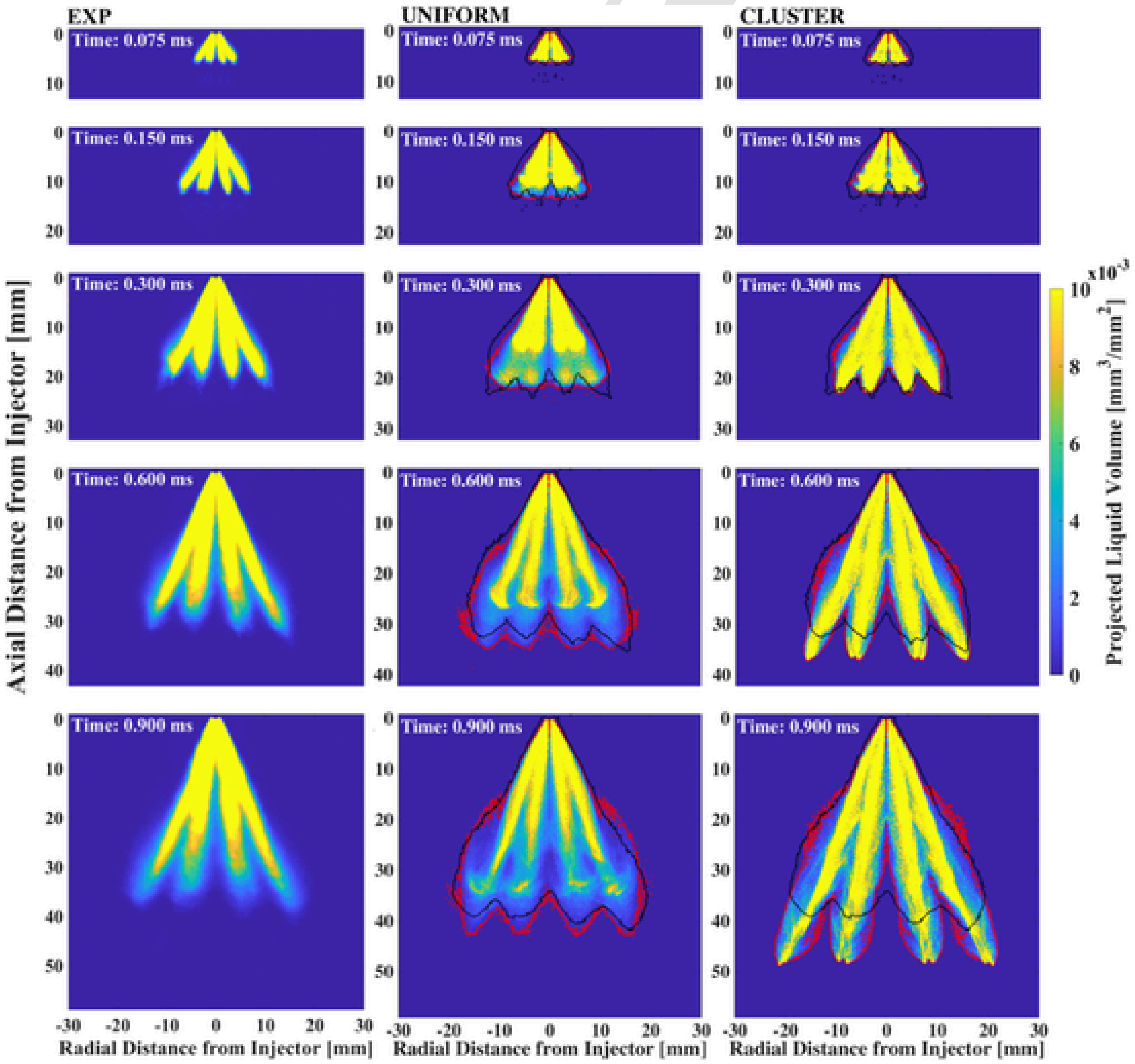

Fig. 27. Effect of the parcel distribution when using optimized breakup model calibrations. Even after calibrating the breakup model using the "cluster" distribution the spray morphology was not well captured. The increased axial component of the droplet velocity is likely too large to allow for an axial decay in PLV and higher evaporation as observed using the "uniform" distribution.

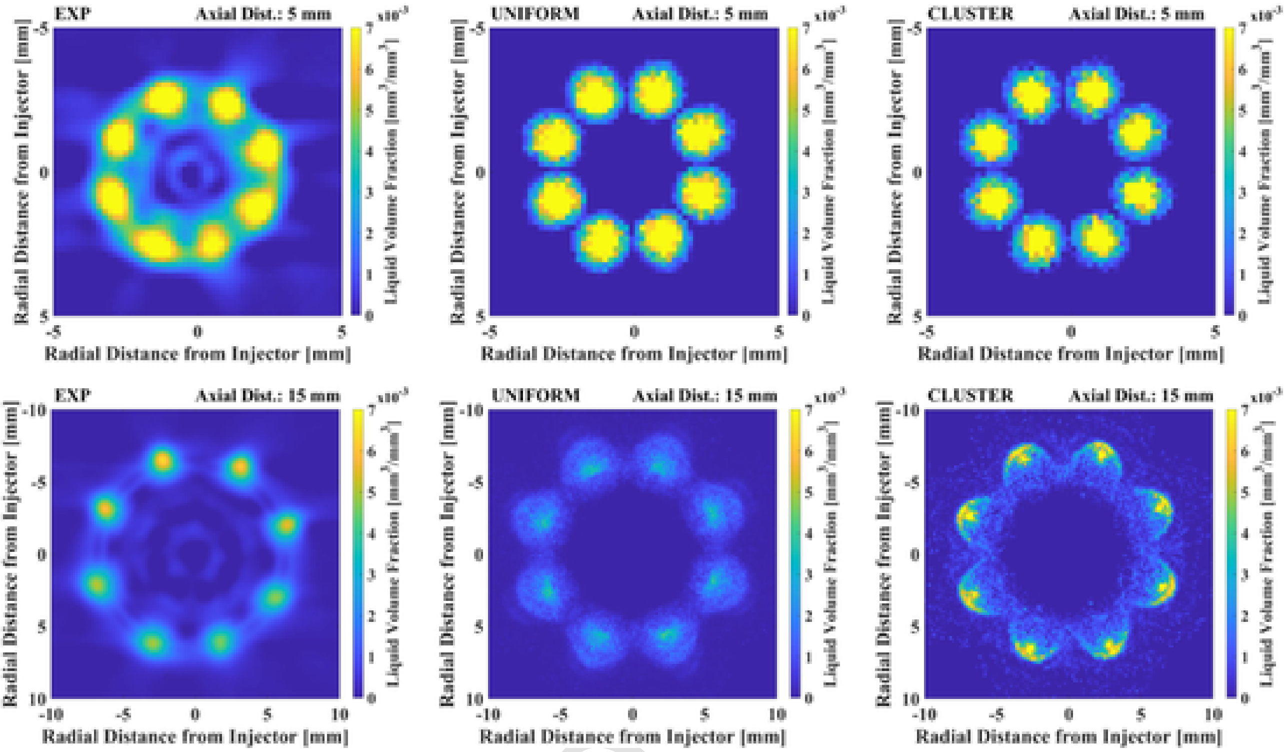

Fig. 28. LVF plume structures when using the calibrated breakup models for each distribution. At Z = 5 mm, the impact of the “cluster” distribution reduces to the plume diameter. After the breakup model calibration both distritbutions are able to qualitatively capture the plume structure.

Finally, in Figure 29, the LVF results are quantitatively compared at axial distances of 5, 15, 20, and 30 mm using both the “uniform” and “cluster” distributions. This comparison reveals that there is a notable improvement in LVF prediction using both distributions when compared to the baseline case (Fig. 10). The “uniform” distribution performs better in the near-field, which is a contrast to the baseline case. On the other hand, the “cluster” distribution shows better performance at 15 and 20 mm. However, at an axial distance of 30 mm, both distributions fail to capture the LVF trends. It is important to consider that LVF data is only available up to axial distances of 30 mm.

These results indicate that the choice of parcel distribution should align with the specific simulation objectives. If the focus is on predicting the near-injector region behavior of a GDI spray, the “cluster” distribution appears to provide results that better represent experimental observations in that region. On the other hand, if the goal is to capture the overall spray morphology, mixing and impingement behavior, which are significantly influenced by the far field region, the “uniform” distribution is a better choice. It better reproduces the experimentally observed overall morphology, LPL, and evaporation. Additionally, these findings highlight the importance of the near-field phenomenon on the overall spray behavior and underscore the significance of making appropriate assumptions when internal flow simulations are not incorporated into the simulation.

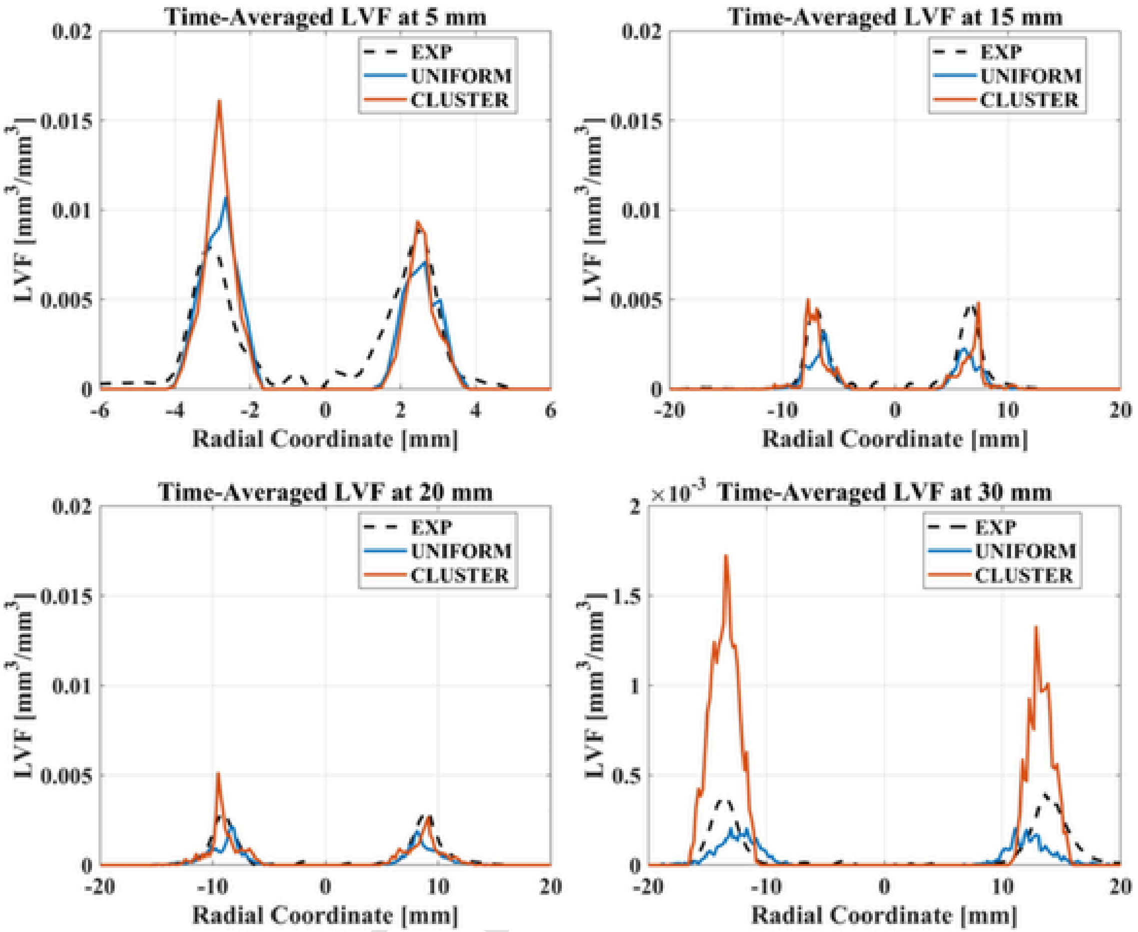

Fig. 29. LVF profiles at $z = 5$, 15, 20, and 30 mm from the injector tip. Contrary to Fig. 10, the "uniform" distribution after the breakup model calibration performs better in the near field. Beyond 30 mm, both distributions fail to capture LVF data.

A.3. Effect of droplet heat transfer coefficient

The sensitivity analysis of the droplet heat transfer coefficient scaling factor on the spray characteristics was performed in this sub-section. Figure 30 shows simulation results for three scaling factors: 1x (no scaling), +5x, and + 10x. As expected, increasing the droplet heat transfer coefficient leads to enhanced evaporation, resulting in a reduction in PLV in the simulation results. This reduction is evident in the faster axial decay of the PLV and the emergence of more distinct and narrower spray plumes. This increased evaporation is particularly notable in regions at axial distances greater than 10 mm, with negligible effects in the near-field region.

Figure 31 shows that the increased evaporation significantly impacts LPL, particularly at times later than 0.5 ms aSOI. The impact on LFW at 5 mm is negligible but becomes substantial at axial distances of 15 and 25 mm. It is important to note that the effect of scaling droplet heat transfer coefficient decreases as the scaling values increase, as indicated in Figure 31. However, it is crucial that the use of this parameter should only be justified when there are uncertainties in the fuel's physical properties or surrogate formulation. If discrepancies arise with well-characterized fuels (e.g., *iso*-octane), other parameters or submodels should be examined.

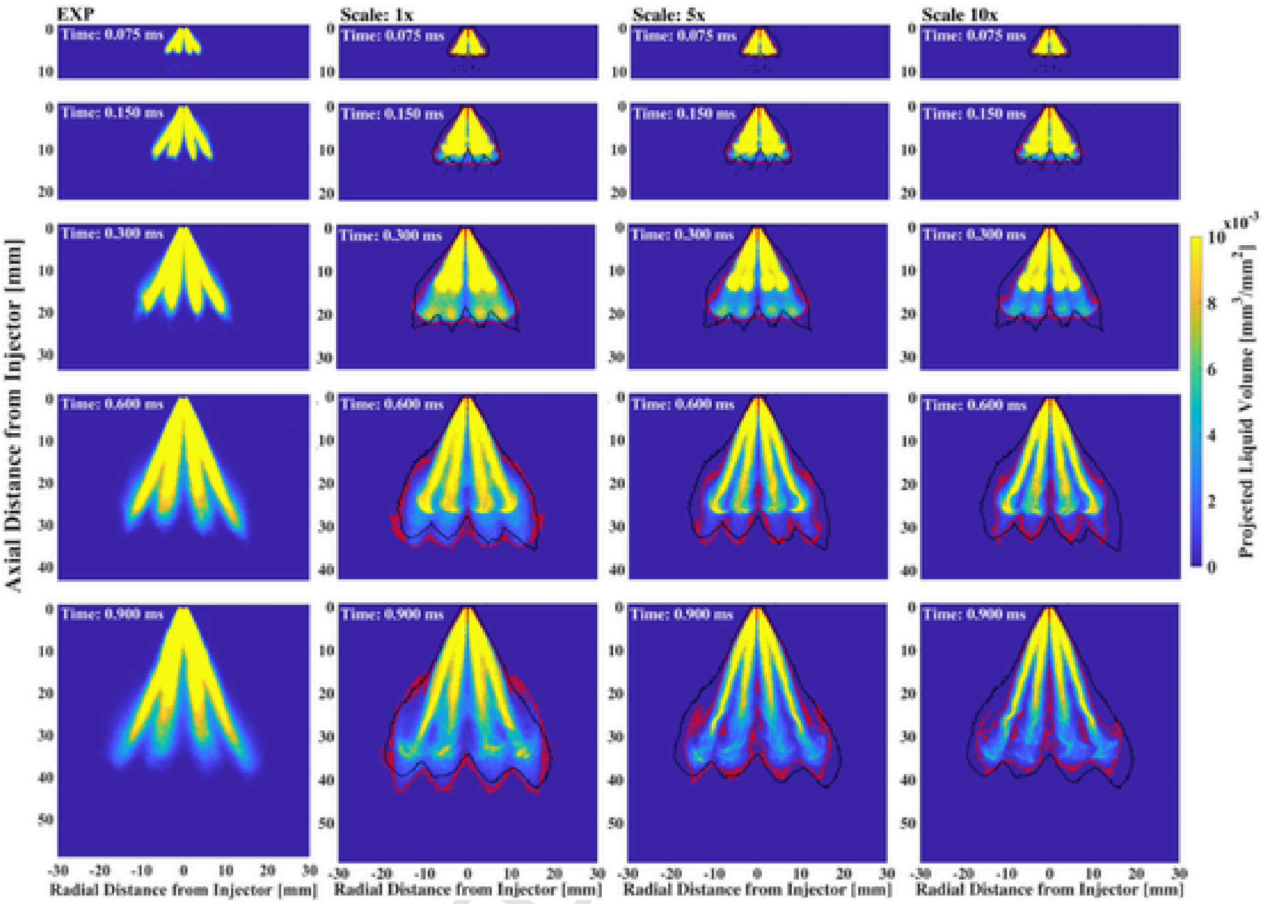

Fig. 30. Impact of the increased droplet heat transfer coefficient on the spray morphology. Increased heat transfer leads to a faster axial decay in the PLV. The mid and far-fields are more sensitive to the increased heat transfer coefficients.

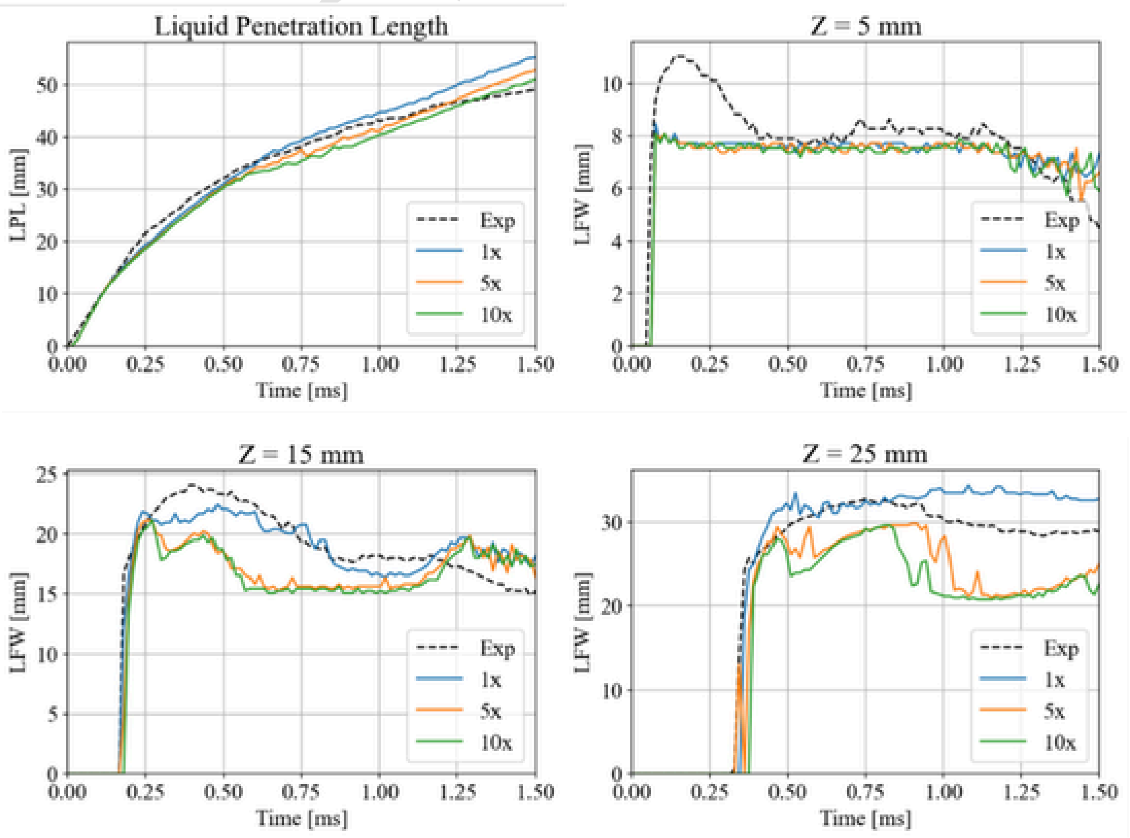

Fig. 31. Impact of the increased heat transfer coefficient on the LPL and LFW. As expected, increasing the heat transfer coefficient decreases both LPL and LFW. Its impact is reduced with increasing multipliers.

A.4. Droplet collision Models: O'Rourke and NTC

The expected number of droplet collisions in a cell over a time interval Δt can be estimated by summing the probability of all possible collisions:

$$M_{coll} = \frac{1}{2}\sum_{i=1}^{N}\sum_{j=1}^{N}\frac{v_{i,j}\sigma_{i,j}\Delta t}{V}$$

Where N is the number of droplets, $v_{i,j}$ is the relative velocity between the two droplets, $\sigma_{i,j}$ is the collision cross section of the two droplets, and V is the cell volume. By grouping droplets of identical properties into parcels, the O'Rourke droplet collision model statistically represents the number of droplet collisions as:

$$M_{coll} = \frac{1}{2}\sum_{i=1}^{N_p} q_i \sum_{j=1}^{N_p}\frac{q_j v_{i,j}\sigma_{i,j}\Delta t}{V}$$

Where N_p is the number of parcels and $q_{i,j}$ is the number of droplets in the parcel. Thus, the evaluation of the number of all possible collisions between parcels will scale with the squared number of parcels due to the double summation. On the other hand, the NTC model evaluates this double summation using a subset of the parcel population. This subset is defined as:

$$M_{cand} = \frac{N_p^2 (q v \sigma)_{\max}\Delta t}{2V}$$

The summation over this subset of parcels is then defined as:

$$M_{coll} = \sum_{i=1}^{\sqrt{M_{cand}}} q_i \sum_{j=1}^{\sqrt{M_{cand}}}\frac{q_j v_{i,j}\sigma_{i,j}\Delta t}{(q v \sigma)_{\max}}$$

Therefore, the term $(q v \sigma)_{\max}$ is used to scale the subset size used to evaluate the number of collisions, resulting in a linear cost increase with the number of parcels.

More information about these two models, as well as collision meshes and outcomes can be found in the literature [38,45,47,48].

References

[1] Knop V, Essayem E. Comparison of PFI and DI operation in a downsized gasoline engine. SAE Int J Engines 2013;6(2):941–52.

[2] Alkidas A.C, Tahry S.H.E. Contributors to the fuel economy advantage of DISI engines over PFI engines. SAE Technical Papers 2003. https://doi.org/10.4271/2003-01-3101.

[3] Jang J, Lee J, Kim J, Park S. Comparisons of the nanoparticle emission characteristics between GDI and PFI vehicles. J Nanopart Res 2015;17(12):1–14. https://doi.org/10.1007/S11051-015-3280-2/FIGURES/10.

[4] Choi K, Kim J, Ko A, Myung C.L, Park S, Lee J. Size-resolved engine exhaust aerosol characteristics in a metal foam particulate filter for GDI light-duty vehicle. J Aerosol Sci 2013;57:1–13. https://doi.org/10.1016/J.JAEROSCI.2012.11.002.

[5] Köpple F, Seboldt D, Jochmann P, Hettinger A, Kufferath A, Bargende M. Experimental investigation of fuel impingement and spray-cooling on the piston of a GDI engine via instantaneous surface temperature measurements. SAE Int J Engines 2014;7(3):1178–94.

[6] Ketterer J.E, Cheng W.K. On the nature of particulate emissions from DISI engines at cold-fast-idle. SAE Int J Engines 2014;7(2):986–94.

[7] Jiang C, Xu H, Srivastava D, Ma X, Dearn K, Cracknell R, et al. Effect of fuel injector deposit on spray characteristics, gaseous emissions and particulate matter in a gasoline direct injection engine. Appl Energy 2017;203:390–402. https://doi.org/10.1016/J.APENERGY.2017.06.020.

[8] Kim N, Chung J, Kim J, Cho S, Min K. Effect of injection parameters on combustion and emission characteristics under catalyst heating operation in a direct-injection spark-ignition engine. Energy Convers Manag 2022;252:115059. https://doi.org/10.1016/J.ENCONMAN.2021.115059.

[9] Bonandrini G, Gioia R.D, Papaleo D, Venturoli L. Numerical study on multiple injection strategies in DISI engines for particulate emission control. SAE Technical Papers 2012. https://doi.org/10.4271/2012-01-0400.

[10] Roberts A, Brooks R, Shipway P. Internal combustion engine cold-start efficiency: a review of the problem, causes and potential solutions. Energy Convers Manag 2014;82:327–50.

[11] Ravindran A.C, Kokjohn S.L. The challenges of using detailed chemistry model for simulating direct injection spark ignition engine combustion during cold-start. Int J Engine Res 2023;24(1):161–77.

[12] Guzzo, M.E., Barros, J.E.M., Júnior, C.A.G., Costa, R.B.R. da, Franco, R.L., and Rodrigues Filho, F.A., "Analysis of ethanol spray behavior into a Single Cylinder Optical Research Engine," 2020.

[13] Köpple F, Jochmann P, Kufferath A, Bargende M. Investigation of the parameters influencing the spray-wall interaction in a GDI engine-prerequisite for the prediction of particulate emissions by numerical simulation. SAE Int J Engines 2013;6(2):911–25.

[14] Rodriguez J.F, Cheng W.K. Analysis of NOx emissions during crank-start and cold fast-idle in a GDI engine. SAE Int J Engines 2017;10(2):646–55.

[15] Bonatesta F, La S, Rocca, Hopkins E, Bell D. Application of computational fluid dynamics to explore the sources of soot formation in a gasoline direct injection engine. SAE Technical Papers 2014. https://doi.org/10.4271/2014-01-2569.

[16] Su J, Xu M, Yin P, Gao Y, Hung D. Particle number emissions reduction using multiple injection strategies in a boosted spark-ignition direct-injection (SIDI) gasoline engine. SAE Int J Engines 2014;8(1):20–9. https://doi.org/10.4271/2014-01-2845.

[17] Zheng Z, Tian X, Zhang X. Effects of split injection proportion and the second injection time on the mixture formation in a GDI engine under catalyst heating mode using stratified charge strategy. Appl Therm Eng 2015;84:237–45. https://doi.org/10.1016/J.APPLTHERMALENG.2015.03.041.

[18] Lucchini T, D'Errico G, Onorati A, Bonandrini G, Venturoli L, Gioia R.D. Development and application of a computational fluid dynamics methodology to predict fuel-air mixing and sources of soot formation in gasoline direct injection engines. Int J Engine Res 2014;15(5):581–96. https://doi.org/10.1177/1468087413500297/ASSET/IMAGES/LARGE/10.1177_1468087413500297-FIG20.JPEG.

[19] Kim J, Chung J, Kim N, Cho S, Lee J, Oh S, et al. Numerical investigation of soot emission sources in a direct-injection spark-ignition engine based on comprehensive breakup model validation. Int J Engine Res 2023;24(1):217–39. https://doi.org/10.1177/14680874211047524/ASSET/IMAGES/LARGE/10.1177_14680874211047524-FIG20.JPEG.

[20] Liquid Penetration Length – Engine Combustion Network, https://ecn.sandia.gov/gasoline-spray-combustion/experimental-diagnostics/liquid-penetration-length/, Oct. 2023.

[21] Paredi D, Lucchini T, D'Errico G, Onorati A, Pickett L, Lacey J. Validation of a comprehensive computational fluid dynamics methodology to predict the direct injection process of gasoline sprays using Spray G experimental data. Int J Engine Res 2020;21(1):199–216. https://doi.org/10.1177/1468087419868020/ASSET/IMAGES/LARGE/10.1177_1468087419868020-FIG20.JPEG.

[22] Pati A, Paredi D, Lucchini T, Hasse C. CFD modeling of gas-fuel interaction and mixture formation in a gasoline direct-injection engine coupled with the ECN spray G injector. SAE Technical Papers 2020. https://doi.org/10.4271/2020-01-0327.

[23] Hwang J, Weiss L, Karathanassis I.K, Koukouvinis P, Pickett L.M, Skeen S.A. Spatio-temporal identification of plume dynamics by 3D computed tomography

using engine combustion network spray G injector and various fuels. Fuel 2020;280:118359.

[24] Sforzo B, Tekawade A, Matusik K, Kastengren A, Ilavsky J, Fezzaa K, et al. X-ray characterization and spray measurements of ECN spray G using alternative fuels under flashing conditions. ILASS Americas 2019.

[25] Blessinger M, Manin J, Skeen S.A, Meijer M, Parrish S, Pickett L.M. Quantitative mixing measurements and stochastic variability of a vaporizing gasoline direct-injection spray. Int J Engine Res 2015;16(2):238–52.

[26] Lucchini T. “Topic 8: Evaporative Spray G (external, plume interaction, flash boiling)”, *ECN8 Proceedings*. Rochester, MI: Engine Combustion Network; 2022.

[27] Lehnert, B., Weiss, L., Berrocal, E., and Wensing, M., “Tomographic reconstruction of spray evolution considering multiple light scattering effects: Characterization of an ECN Spray G Injector,” *10th International Conference on Modeling and Diagnostics for Advanced Engine Systems, COMODIA 2022*, 337–345, 2022.

[28] Duke D.J, Kastengren A.L, Matusik K.E, Swantek A.B, Powell C.F, Payri R, et al. Internal and near nozzle measurements of Engine Combustion Network ‘Spray G’ gasoline direct injectors. Exp Therm Fluid Sci 2017;88:608–21. https://doi.org/10.1016/J.EXPTHERMFLUSCI.2017.07.015.

[29] Duke D.J, Swantek A.B, Sovis N.M, Tilocco F.Z, Powell C.F, Kastengren A.L, et al. Time-resolved x-ray tomography of gasoline direct injection sprays. SAE Int J Engines 2016;9(1):143–53.

[30] Kastengren A.L, Tilocco F.Z, Duke D, Powell C.F, Zhang X, Moon S. Time-resolved x-ray radiography of sprays from engine combustion network spray a diesel Injectors. Atomization Sprays 2014;24(3):251–72. https://doi.org/10.1615/ATOMIZSPR.2013008642.

[31] Kastengren A, Powell C.F. Synchrotron X-ray techniques for fluid dynamics. Exp Fluids 2014;55(3):1–15. https://doi.org/10.1007/S00348-014-1686-8/METRICS.

[32] Richards K.J, Senecal P.K, Pomraning E. CONVERGE 2022;3.

[33] Park J.-W, Mandhapati R, Zhang A, Zhao L, Pei Y, Mittal A, et al. Numerical Investigation of Differential Evaporation of Multi-Component Gasoline Surrogate Fuels. 13th US. College Station, TX: National Combustion Meeting; 2023.

[34] Kalvakala K, et al. Numerical Investigation of Spray Characteristics in a Direct-Injection Spark-Ignition Engine Under Cold Conditions. Indianapolis, IN: American Society of Mechanical Engineers; 2022.

[35] Reitz R.D, Diwakar R. Structure of high-pressure fuel sprays. SAE Trans 1987;492–509.

[36] Patterson M.A. Modeling the effects of fuel injection characteristics on diesel combustion and emissions. The University of Wisconsin-Madison; 1997.

[37] Torelli R, D’Errico G, Lucchini T, Ikonomou V, McDavid R.M. A spherical volume interaction DDM approach for diesel spray modeling. Atomization Sprays 2015;25(4).

[38] O’rourke P.J. Collective drop effects on vaporizing liquid sprays. Princeton University; 1981.

[39] Dahms R.N, Oefelein J.C. The significance of drop non-sphericity in sprays. Int J Multiph Flow 2016;86:67–85. https://doi.org/10.1016/J.IJMULTIPHASEFLOW.2016.07.010.

[40] Nguyen T.M, Dahms R.N, Pickett L.M, Tagliante F. The Corrected Distortion model for Lagrangian spray simulation of transcritical fuel injection. Int J Multiph Flow 2022;148:103927.

[41] Amsden, A.A., O’Rourke, P.J., and Butler, T.D., “KIVA-II: A computer program for chemically reactive flows with sprays,” 1989, doi:10.2172/6228444.

[42] Guo H, Torelli R, Szybist J.P, Som S. CFD modeling of pre-spark heat release in a boosted direct-injection spark-ignition engine. Int J Engine Res 2023;24(1):3–15. https://doi.org/10.1177/14680874211044110/ASSET/IMAGES/LARGE/10.1177_14680874211044110-FIG12.JPEG.

[43] Launder B.E, Spalding D.B. The numerical computation of turbulent flows. Numerical Prediction of Flow, Heat Transfer Turbulence and Combustion 1983; 96–116. https://doi.org/10.1016/B978-0-08-030937-8.50016-7.

[44] Yakhot V, Orszag S.A. Renormalization group analysis of turbulence. I. Basic theory. J Sci Comput 1986;1(1):3–51. https://doi.org/10.1007/BF01061452/METRICS.

[45] Post S.L, Abraham J. Modeling the outcome of drop–drop collisions in Diesel sprays. Int J Multiph Flow 2002;28(6):997–1019.

[46] Torelli R, Scarcelli R, Som S, Zhu X, Lee S.Y, Naber J, et al. Toward predictive and computationally affordable Lagrangian-Eulerian modeling of spray–wall interaction. Int J Engine Res 2020;21(2):263–80. https://doi.org/10.1177/1468087419870619/FORMAT/EPUB.

[47] Schmidt D.P, Rutland C.J. A new droplet collision algorithm. J Comput Phys 2000;164(1):62–80.

[48] Hou S. Investigation of the interaction mechanisms between closely spaced sprays from micro-hole nozzles. University of Massachusetts Amherst 2005.

[49] Reitz R, et al. Modeling atomization processes in high-pressure vaporizing sprays. Atomisation and Spray Technology 1987;3(4):309–37.

[50] Pope, S.B., “An explanation of the turbulent round-jet/plane-jet anomaly,” *Https://Doi.Org/10.2514/3.7521* 16(3):279–281, 2012, doi:10.2514/3.7521.

[51] Maes N, Dam N, Somers B, Lucchini T, D’Errico G, Hardy G. Experimental and numerical analyses of liquid and spray penetration under heavy-duty diesel engine conditions. SAE Int J Fuels Lubr 2016;9(1):108–24.